

An analytical multiphase flow model for parallel plate electrolyzers

Rajora, A.; Haverkort, J. W.

DOI

[10.1016/j.ces.2022.117823](https://doi.org/10.1016/j.ces.2022.117823)

Publication date

2022

Document Version

Final published version

Published in

Chemical Engineering Science

Citation (APA)

Rajora, A., & Haverkort, J. W. (2022). An analytical multiphase flow model for parallel plate electrolyzers. *Chemical Engineering Science*, 260, Article 117823. <https://doi.org/10.1016/j.ces.2022.117823>

Important note

To cite this publication, please use the final published version (if applicable). Please check the document version above.

Copyright

Other than for strictly personal use, it is not permitted to download, forward or distribute the text or part of it, without the consent of the author(s) and/or copyright holder(s), unless the work is under an open content license such as Creative Commons.

Takedown policy

Please contact us and provide details if you believe this document breaches copyrights. We will remove access to the work immediately and investigate your claim.



An analytical multiphase flow model for parallel plate electrolyzers

A. Rajora, J.W. Haverkort

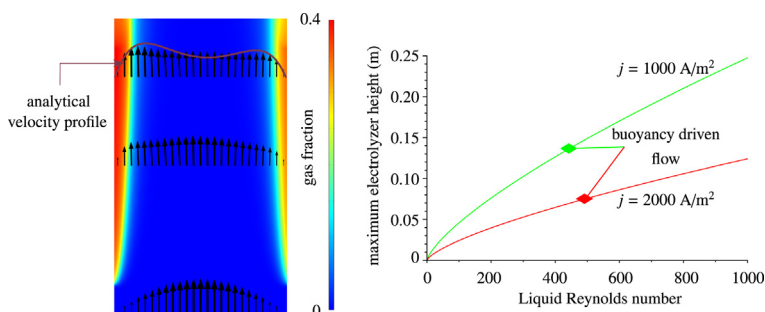
Process & Energy Department, Delft University of Technology, Leeghwaterstraat 39, 2628 CB Delft, the Netherlands



HIGHLIGHTS

- We present a fully analytical multiphase flow model of a parallel plate electrolyzer.
- Validated analytical expressions for velocity and gas fraction profiles are provided.
- The maximum allowable height to avoid significant gas crossover is quantified.
- Natural convection can be efficiently used up to several centimeters.
- Higher pressure, forced flow or small bubbles allow significantly larger heights.

GRAPHICAL ABSTRACT



ARTICLE INFO

Article history:

Received 19 January 2022
 Received in revised form 15 June 2022
 Accepted 17 June 2022
 Available online 27 June 2022

Keywords:

Multiphase flow
 Water electrolysis
 Membraneless
 Analytical solution
 Parallel plate electrolyzer

ABSTRACT

Membraneless parallel-plate electrolyzers use electrolyte flow to avoid product crossover. Using a mixture model neglecting inertia, and assuming an exponential gas fraction profile, we derive approximate analytical expressions for the velocity profile and pressure drop for thin plumes. We verify these expressions using numerical solutions obtained with COMSOL and validate them using experimental data from the literature. We find that the wall gas fraction increases rapidly at small heights, but becomes fairly constant at larger heights. These expressions serve as a guiding framework for designing a membraneless parallel-plate electrolyzer by quantifying the maximum possible height. We find that buoyancy driven membraneless parallel-plate electrolyzers with a 3 mm gap can be designed with a maximum height of around 7.6 cm at 1000 A/m² for operation with 98% product purity at atmospheric pressure. For a forced flow at Re = 1000, the same electrolyzer can be made around 17.6 cm tall at 1000 A/m². These limits can be further improved with smaller bubbles or higher pressure.

© 2022 The Author(s). Published by Elsevier Ltd. This is an open access article under the CC BY license (<http://creativecommons.org/licenses/by/4.0/>).

Introduction

Green hydrogen can be produced by splitting water in electrolyzers using electricity from renewable sources. Traditionally, a membrane or a separator is used between the cathode and the anode that allows the transport of ions and separates the gaseous products. However, these membranes and separators are susceptible to degradation (O'Neil et al., 2016), gas crossover (Millet et al.,

2011) or blockage in the presence of impurities (Tong et al., 2020) reducing the durability of the electrolyzer.

Membraneless electrolyzers have been studied as one of the promising alternatives to existing electrolyzer technologies. Various designs for membraneless operation of electrochemical cells have been studied including flow-through porous electrodes (O'Neil et al., 2016; Gillespie et al., 2015; Esposito, 2017; Rajaei et al., 2021; Obata et al., 2021) and flow-by electrodes (Hashemi et al., 2015; Davis et al., 2018; Suss et al., 2016; Hadikhani et al., 2021; Holmes-Gentle et al., 2017). Esposito (2017) provides a good overview of challenges and opportunities for membraneless

E-mail addresses: A.Rajora@tudelft.nl (A. Rajora), J.W.Haverkort@tudelft.nl (J.W. Haverkort)

Nomenclature

Dimensionless variables

$\bar{\delta}$	dimensionless plume thickness = $\frac{\delta}{l}$
ε	gas fraction

Greek variables

δ	e-folding plume thickness, [m]
μ	liquid dynamic viscosity, [Pa s]
ρ	liquid density, [kg/m ³]

Subscripts and other notation

0	properties at $x = 0$
\mathbf{U}	superficial velocity vector given by $U\hat{\mathbf{x}} + W\hat{\mathbf{z}}$
a	anode
c	cathode
g	gaseous phase
max	maximum value of the variable
m	mixture
nc	properties for flow due to natural convection
$\hat{\mathbf{x}}$	unit vector in horizontal direction
$\hat{\mathbf{z}}$	unit vector in vertical direction
\mathbf{u}	interstitial velocity vector given by $u\hat{\mathbf{x}} + w\hat{\mathbf{z}}$

Symbols

$\langle W \rangle$	average vertical superficial liquid velocity, [m/s]
\mathcal{A}	dimensional constant in $\delta = \mathcal{A} \frac{z^a}{\langle W \rangle^b}$, [m ^{1+b-a} /s ^b]
x	wall normal coordinate
z	vertical coordinate
d_b	bubble diameter, [m]
w_b	$\equiv \frac{\rho g l^2}{12\mu}$, characteristic velocity due to buoyancy, [m/s]
ν_m	molar volume, [m ³ /mol]
$\langle W_g \rangle$	average vertical superficial gas velocity, [m/s]
g	acceleration due to gravity, [m/s ²]
h	height of the electrode, [m]
j	current density, [A/m ²]
l	inter-electrode gap, [m]
P	reduced pressure = $p + \rho g z$, [Pa]
p	pressure, [Pa]
T	temperature, [K]
U_g	horizontal superficial gas velocity, [m/s]
w	vertical interstitial velocity, [m/s]
w_p	$\equiv -\frac{\partial p}{\partial z} \frac{l^2}{12\mu}$, characteristic velocity due to pressure gradient, [m/s]
Re	Reynolds number

electrolyzers. In this paper, we deal with electrolyzers without a separator, diaphragm or membrane, where the flow is parallel to the electrodes. Such electrolyzers may offer potential reduction in costs and ohmic resistance.

Previous experimental studies have focused on demonstrating the use of flow to mitigate gas crossover (Gillespie et al., 2015; Hashemi et al., 2015; Davis et al., 2018; Holmes-Gentle et al., 2017; Pang et al., 2020). Pang et al. (2020) recently made the first attempt to systematically explore the performance limits and trade-offs between various parameters such as current density, efficiency, product purity, and electrode size in membraneless parallel plate electrolyzers. In the past, many researchers studied the gas evolution between vertical electrodes with narrow interelectrode gap using experiments (Boissonneau and Byrne, 2000; Kuroda et al., 2008; Hreiz et al., 2015; Aldas et al., 2008; Riegel et al., 1998; Lee et al., 2019) and numerical simulations (Obata et al., 2021; Wedin and Dahlkild, 2001; Schillings et al., 2015; Le Bideau et al., 2020; Zarghami et al., 2020; Rodríguez and Amores, 2020; Mat and Aldas, 2005) to investigate the two-phase hydrodynamics. Very few researchers made an attempt to analytically model the two-phase flow in a membraneless parallel plate electrolyzer (Schillings et al., 2015; Gol'dberg, 2002; Vogt, 1999; Czarnetzki, 1989; Riviere and Cartellier, 1999).

In this work, we develop an analytical model for a membraneless parallel plate electrolyzer without a separator, see Fig. 1. We first introduce a numerical model to simulate the multiphase flow under laminar flow conditions in Section 2. Using the insights from the numerical model and governing equations, we derive approximate analytical expressions in Section 3 for the velocity profile, superficial velocity, shear stress, and pressure drop. Finally, we provide an expression for the maximum height of the electrolyzer based on interelectrode gap and flow conditions in Section 5.

Mathematical Model

Model Configuration

Fig. 1 shows a configuration of a membraneless parallel plate electrolyzer. The coordinates z and x represent the vertical and

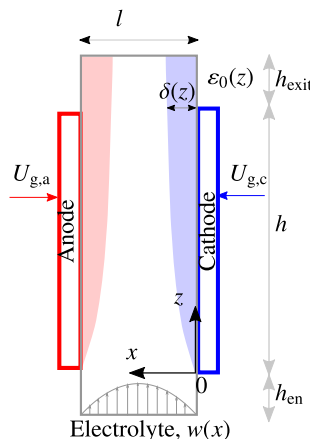


Fig. 1. Configuration of a membraneless parallel plate electrolyzer. The gas bubbles are generated at the electrode surface and move in a plume of e-folding width δ . The wall gas fraction is denoted by ε_0 . The liquid electrolyte moves vertically with interstitial velocity $w(x)$.

wall-normal directions, respectively. The vertical electrodes have a height h and are assumed to have a depth much larger than the interelectrode gap l . This allows us to represent the electrolyzer in 2D. The bubbles in the electrolyzer move in a plume of e-folding thickness $\delta(z)$, which is expected to become thicker with height as more gas is generated. The wall gas fraction on the electrode surface is denoted by ε_0 . The liquid electrolyte enters with a vertical interstitial velocity $w(x)$ because of forced flow or buoyancy due to the presence of the bubbles. The heights for the entrance region and the exit region are denoted by h_{en} and h_{exit} .

Numerical Model

We model the two-phase hydrodynamics for laminar flow in the electrochemical cell with the mixture model formulation (Ishii, 1975; Wedin and Dahlkild, 2001; Schillings et al., 2015) using COMSOL Multiphysics v5.6, update 2 (CFD, 2020). The mix-

ture model formulation is valid when the gaseous phase is in equilibrium with the liquid phase. This is a reasonable approximation for small electrochemical bubbles that have a much smaller density than that of the liquid electrolyte. We assume that the gas bubbles are spherical due to their small diameter d_b and that the presence of high molarity electrolytes prevents coalescence (Orvalho et al., 2021; Kreysa and Kuhn, 1985; Lessard and Zieminski, 1971). The velocities of the liquid phase and the gas phase are denoted by \mathbf{u} and \mathbf{u}_g , respectively, while the gas fraction is denoted by ε . The mixture dynamic viscosity $\mu_m = \mu\mu_r = \frac{\mu}{1-\varepsilon}$ (Ishii and Zuber, 1979), where μ is the dynamic viscosity of the liquid electrolyte and $\mu_r = \frac{1}{1-\varepsilon}$. The mixture density $\rho_m = (1-\varepsilon)\rho + \varepsilon\rho_g$ where ρ_g and ρ are the densities of the gaseous and the liquid phase, respectively. Note that we do not use any subscript for the properties corresponding to the liquid phase, but use subscript 'g' for the properties corresponding to the gaseous phase. The continuity equation for the mixture in steady state is

$$\nabla \cdot (\rho_m \mathbf{U}_m) = 0, \quad (1)$$

and the momentum equation for the mixture at steady state is

$$\rho_m \mathbf{U}_m \cdot \nabla \mathbf{U}_m = -\nabla p + \nabla \cdot \left(\mu_m \left(\nabla \mathbf{U}_m + (\nabla \mathbf{U}_m)^T \right) \right) - \rho_m g \hat{\mathbf{z}}, \quad (2)$$

where $\mathbf{U}_m = (1-\varepsilon)\mathbf{u} + \varepsilon\mathbf{u}_g = \mathbf{u} + \varepsilon\mathbf{u}_s$ is the superficial mixture viscosity. The difference between the gas and the liquid interstitial velocity is the slip velocity $\mathbf{u}_s \equiv \mathbf{u}_g - \mathbf{u}$. Riviere and Cartellier (1999) use a different closure relation for shear stress giving μ instead of μ_m in the second term of Eq. (2). However, past works show that the effective mixture viscosity increases with an increase in gas fraction, and even diverges above a certain maximum gas fraction (Krieger and Dougherty, 1959; Jamshidi et al., 2019; Li et al., 2022). Nonetheless, In this work we have provided relations for both cases – a constant mixture viscosity case in the main text and a gas fraction dependent increasing mixture viscosity in Appendix A.

The continuity equation for the gaseous phase for laminar flow in steady state assuming constant gas density, using $\mathbf{U}_s = \varepsilon(1-\varepsilon)\mathbf{u}_s$, can be rewritten as

$$\mathbf{U}_m \cdot \nabla \varepsilon = -\nabla \cdot \mathbf{U}_s. \quad (3)$$

We describe the relative motion of the gas bubbles as the superposition of relative motion due to various phenomena by writing

$$\mathbf{u}_s = \mathbf{u}_{St} + \mathbf{u}_{Sa} + \mathbf{u}_{Hd} + \mathbf{u}_{Sd} + \mathbf{u}_{Sm}. \quad (4)$$

In Eq. (4), we expressed the total slip velocity as a superposition of five different components. We describe below the physical meaning of each of these slip velocities. The first term \mathbf{u}_{St} arises due to the balance between buoyancy and drag force and gives a slip velocity equal to the rise velocity of the bubble in liquid, $\mathbf{u}_{St} = f(\varepsilon) \frac{\rho g d_b^2}{18\mu} \hat{\mathbf{z}}$. Here, $f(\varepsilon) = (1-\varepsilon)^4$ is a hindrance function for a swarm of particles (Richardson and Zaki, 1954; Nicolai et al., 1995). Note that we used a power 4 in the hindrance function to give expressions similar to Schillings et al., 2015, while Richardson and Zaki, 1954) and Nicolai et al., 1995 find a slightly higher power of 4.65 and 5, respectively. However, we checked our simulations with these slightly higher powers in the hindrance function and find negligible differences in the numerical results. There have been some other works which suggest that the bubble swarm velocities may be higher than for a single isolated bubble (Kellermann et al., 1998; Kreysa and Kuhn, 1985; Sigrist et al., 1980). The exact expression for $f(\varepsilon)$ is, therefore, debatable. Smaller powers of $(1-\varepsilon)$ in $f(\varepsilon)$ would make the gas plumes more exponential in shape, leading to a better accuracy of our model. The drag force is assumed to be

Stokes' drag, which is valid for $w_{St} = f(\varepsilon) \frac{\rho^2 g d_b^3}{18\mu^2} \ll 1$. For $\varepsilon \rightarrow 0$, this corresponds to a bubble diameter of approximately 100 μm . However, with higher gas fractions usually observed in electrolyzers, the error becomes smaller for larger bubble diameters.

The second term \mathbf{u}_{Sa} corresponds to the Saffman lift force experienced by the particles translating and rotating in a velocity gradient (Saffman, 1965; McLaughlin, 1991; Mei, 1992). The Saffman lift acts in a direction perpendicular to the vorticity vector and the slip velocity vector. In a buoyancy driven flow, $\frac{\partial w}{\partial x} \gg \frac{\partial u}{\partial z}$ and the slip velocity due to buoyancy is dominant in the vertical direction. So, as a simplification, we assume that the Saffman lift force is

given by $\mathbf{u}_{Sa} = -0.17w_{St} \sqrt{\frac{d_b^2}{\mu} \left| \frac{\partial w}{\partial x} \right|} \text{sign} \left(\frac{\partial w}{\partial x} \right) \hat{\mathbf{x}}$ (Saffman, 1965) and acts only in the wall-normal direction. The Saffman lift force tends to push the bubbles from a region of high velocity to a region of low velocity. It should be noted that here we neglected the vertical component of the Saffman lift force because it is expected to be much smaller than w_{St} . The third term \mathbf{u}_{Hd} is due to collision-like interaction between bubbles, similar to hydrodynamic self diffusion of suspended particles (Wedin and Dahlkild, 2001; Schillings et al., 2015; Nicolai et al., 1995; Ham and Homsy, 1988; Harada and Otomo, 2009), given by $\mathbf{u}_{Hd} = -\frac{d_b w_{St}}{2} \frac{\mathcal{D} \cdot \nabla \varepsilon}{\varepsilon}$. Here, $\mathcal{D} = \begin{pmatrix} 1 & 0 \\ 0 & 8 \end{pmatrix}$

is a non-isotropic dimensionless dispersion tensor (Nicolai et al., 1995). Inserting the expression of \mathbf{u}_{Hd} in Eq. (3) gives a diffusion term $\nabla \cdot (\mathcal{D}_{Hd} \cdot \nabla \varepsilon)$ with dispersion coefficient $\mathcal{D}_{Hd} = \mathcal{D} \frac{d_b w_{St} (1-\varepsilon)}{2}$. The expression for \mathcal{D}_{Hd} differs from the expression provided by Le Bideau et al., 2020 where the dispersion coefficient is multiplied by an additional factor ε . However, our expression is consistent with the experimentally observed hydrodynamic diffusivities (Nicolai et al., 1995; Ham and Homsy, 1988) where the dispersion coefficient is proportional to $d_b w_{St}$. The dispersion coefficient used in the expression of \mathbf{u}_{Hd} is a consequence of the random path taken by the liquid in the presence of bubbles similar to hydrodynamic dispersion in a porous medium (Perkins and Johnston, 1963; Nguyen and Papavassiliou, 2020) and is not the same as the turbulent eddy viscosity, which we have neglected in this work.

The fourth and the fifth terms, \mathbf{u}_{Sd} and \mathbf{u}_{Sm} , are results of increased bubble–bubble interactions in a sheared flow. This causes movement of bubbles from regions of high gas fraction to low gas fraction, called shear induced diffusion given by

$$\mathbf{u}_{Sd} = -\frac{d_b^2}{4} \left| \frac{\partial w}{\partial x} \right| \frac{\varepsilon(1+0.5e^{8.8\varepsilon})}{3(1-\varepsilon)} \nabla \varepsilon \quad (\text{Leighton and Acrivos, 1987a; Leighton and Acrivos, 1987b}),$$

and from regions of high shear rate to regions of low shear rate, called shear induced migration given by $\mathbf{u}_{Sm} = -\text{sign} \left(\frac{\partial w}{\partial x} \right) \frac{0.15 d_b^2 \varepsilon}{1-\varepsilon} \nabla \left(\frac{\partial w}{\partial x} \right)$ (Leighton and Acrivos, 1987b). All expressions of slip velocities assume that the liquid flow is primarily in the vertical direction. In regions where the flow is not vertical, the slip velocity expressions should be modified. However, as shown later in Fig. 3, we see that for the present configuration, the flow is primarily in the vertical direction. The validity of these expressions for high current density where these bubble–bubble interactions are significant was further established by comparison with four-way coupled DNS simulations for laminar flows in Schillings et al., 2017.

For water electrolysis, producing one mole of hydrogen at the cathode involves transfer of two moles of electrons, while producing one mole of oxygen at the anode involves transfer of four moles of electrons. The volumetric flux, or superficial gas velocity U_g of the electrogenerated gas in the x-direction can be directly related to the applied current density using the Faraday's law as:

$$U_{g,c} = \frac{\mathcal{V}_m}{2F} j, \quad \text{and} \quad U_{g,a} = -\frac{\mathcal{V}_m}{4F} j, \quad (5)$$

where \mathcal{V}_m is the molar volume of the gas. For an ideal gas, $\mathcal{V}_m = RT/p$ where R is the universal gas constant. For simplicity, we assume a 100% gas evolution efficiency (Vogt, 2011). It should be noted that increasing the pressure of the system decreases the molar volume of the gas, thereby reducing the gas flux.

Analytical Model

In this section, we find an approximate analytical solution for Eq. (2) and derive expressions for the velocity profile, average superficial velocity, and pressure drop along the height of the electrode. We will also highlight the assumptions and limits of the analytical solution.

Volume fraction

We assume that the gas fraction in the interelectrode gap can be written as

$$\varepsilon = \varepsilon_0 \left(e^{-\frac{x}{\delta}} + e^{-\frac{l-x}{\delta}} \right), \quad (6)$$

where ε_0 is the gas fraction at the electrode surface and δ is the e-folding plume thickness. Here, we assume equal gas fraction at both electrodes, but treat a more general case of different gas fractions in Appendix A. We also assume that the plume thickness is equal on the cathode and the anode side. This is approximately valid as long as the diameter of the oxygen and the hydrogen are similar. We provide a general solution for different plume thicknesses in Appendix B. Using Eq. (6), the average gas fraction in the electrode gap can be written as

$$\langle \varepsilon \rangle = \frac{2\varepsilon_0\delta \left(1 - e^{-\frac{l}{\delta}} \right)}{l}, \quad (7)$$

which gives $\langle \varepsilon \rangle = \frac{2\varepsilon_0\delta}{l}$ for $\delta \ll l$ and $\langle \varepsilon \rangle = 2\varepsilon_0$ for $\delta \gg l$.

Plume thickness

We assume that the plume thickness can be written as

$$\delta = \frac{\mathcal{A}z^a}{\langle W \rangle^b}, \quad (8)$$

where \mathcal{A} is a dimensional constant depending on the current density, electrolyte, and the electrode. Schillings et al. (2015) conducted an analytical scaling study for natural recirculation when the bubble diffusion coefficient is much smaller than the liquid kinematic viscosity so that bubble diffusion is smaller than momentum diffusion, to give $\delta \sim \left(\frac{\rho g z d_b^6}{\mu U_g} \right)^{1/4}$. At high current density, shear-induced diffusion becomes dominant, and the plume thickness is predicted to be given by $\delta \sim (d_b^2 z)^{1/3}$ (Schillings et al., 2015). Schillings et al. (2015) also showed analytically the well-known L ev eque approximation similarity solution result that for a forced flow, $b = 1/3$. Krikke, 2021 analyzed the existing experimental data of Weier and Landgraf, 2013, Baczyzmaleski et al., 2015, and Aldas et al., 2008 and showed that at low current density and heights, $a \approx 0.5$. Bongenaar-Schlechter et al. (1985) found from both theory and experiments that $a \approx 0.3$ and $b \approx 1/3$ under forced flow conditions. Fukunaka et al. (1989) found experimentally that the bubble layer grows along the vertical height with $a \approx 0.33$ for current densities ranging from 200 A/m² to 1000 A/m², while $a \approx 0.4$ for 100 A/m². Lee et al. (2019) experimentally observed in a forced flow that b ranges from 0.3 to 0.7. Pang et al. (2020) made use of high speed videography and fitted the plume thickness for the region above the electrode with $a = b = 0.47$.

Governing equation and boundary conditions

We assume that inertial forces are negligible in comparison to the sum of pressure forces and buoyancy. It should be noted that for natural recirculation, this assumption may not hold everywhere, especially near the inlet and in the core region where little or no gas is present. Therefore, in such cases, we expect a deviation from the numerical solution. Neglecting the inertial term in the z -component of the momentum equation from Eq. (2), we can write

$$0 = -\frac{\partial P}{\partial z} + \frac{\partial}{\partial x} \left(\mu_m \frac{\partial w}{\partial x} \right) + \varepsilon \rho g, \quad (9)$$

where $P = p + \rho g z$ is the reduced pressure and ε is given by Eq. (6). We used here the limit $\rho_g \ll \rho$, for which $\rho_m = \rho(1 - \varepsilon)$. We also assumed that $w_s \ll w$ for small bubbles, that allows us to write $W_m = w + \varepsilon w_s \approx w$. We now introduce the following dimensionless and characteristic variables:

$$\bar{\delta} = \frac{\delta}{l}, \quad \bar{x} = \frac{x}{l}, \quad w_p = -\frac{\partial P}{\partial z} \frac{l^2}{12\mu} \quad \text{and} \quad w_b = \frac{\rho g l^2}{12\mu}, \quad (10)$$

and rewrite Eq. (9) as

$$0 = 12w_p + \frac{\partial}{\partial \bar{x}} \left(\mu_r \frac{\partial w}{\partial \bar{x}} \right) + 12w_b \varepsilon = 0. \quad (11)$$

To solve Eq. (11), we need two boundary conditions which can be obtained from the no-slip condition for the liquid electrolyte at the electrode surface so that $w = 0$ at $\bar{x} = 0$ and $\bar{x} = 1$.

Electrolyte velocity

In the below analysis, we assume $\mu_r = \frac{\mu_m}{\mu} = 1$ to obtain more transparent equations, but provide a more generally relevant case of $\mu_r = \frac{1}{1-\varepsilon}$ in Appendix A.

Interstitial velocity profile

Solving Eq. 11 with Eq. (6), no-slip boundary conditions and assuming $\mu_m = \mu$, we get

$$w = 6w_p \bar{x}(1 - \bar{x}) + 12w_b \varepsilon_0 \bar{\delta}^2 \left(1 - e^{-\frac{\bar{x}}{\bar{\delta}}} \right) \left(1 - e^{-\frac{1-\bar{x}}{\bar{\delta}}} \right). \quad (12)$$

The first term is the common pressure driven parabolic profile. For large $\bar{\delta} \gg 1$, Eq. (12) tends to $(6w_p + 12w_b \varepsilon_0) \bar{x}(1 - \bar{x})$ so that buoyancy assists the pressure gradient in driving the parabolic flow profile. For thin plumes, in the limit of $\bar{\delta} \ll 1$, the second term describes a plug flow with a constant velocity in the center, decreasing to zero in very thin boundary layers near $\bar{x} = 0$ and $\bar{x} = 1$. In this limit, it can be approximated by $12w_b \varepsilon_0 \bar{\delta}^2 \left(1 - \frac{\cosh((2\bar{x}-1)/2\bar{\delta})}{\cosh(1/2\bar{\delta})} \right)$ similar to the analytical solution for Hartmann flow in a magnetic field (Hartmann, 1934; M uller and B uhler, 2001) and the Darcy-Brinkman equation for flow in a porous medium, in which case $\bar{\delta}$ is the square root of the ratio of permeability and porosity (Vafai and Kim, 1989).

Average superficial velocity

The average superficial velocity, $\langle W \rangle = \int_0^1 w(1 - \varepsilon) d\bar{x}$ using Eq. (12) gives

$$\langle W \rangle = w_p + 12\varepsilon_0 \bar{\delta}^2 (w_b - w_p) \left(1 - 2\bar{\delta} + (1 + 2\bar{\delta}) e^{-\frac{1}{\bar{\delta}}} \right) - 12\varepsilon_0^2 \bar{\delta}^2 w_b \left(\bar{\delta} - 2e^{-\frac{1}{\bar{\delta}}} - \bar{\delta} e^{-\frac{2}{\bar{\delta}}} \right) \quad (13)$$

For thin plumes ($\varepsilon_0 \bar{\delta} \ll 1$ and $e^{-1/\bar{\delta}} \ll 1$) with respect to interelectrode gap, Eq. (13) can be written as

$$\langle W \rangle = w_p + 12w_b \varepsilon_0 \bar{\delta}^2 (1 - 2\bar{\delta}), \quad \left(\begin{array}{l} w_b \gg w_p \text{ or} \\ 12\varepsilon_0 \bar{\delta}^2 \ll 1 \end{array} \right) \quad (14)$$

In the limit of zero gas fraction, $\varepsilon_0 \rightarrow 0$, Eq. (14) reduces to the single phase Hagen–Poiseuille relation, $\langle W \rangle = w_p$. For the homogeneous limit ($\bar{\delta} \gg 1$), the gas fraction uniformly becomes $2\varepsilon_0$ and Eq. (13) gives

$$\langle w \rangle = \frac{\langle W \rangle}{1 - 2\varepsilon_0} = w_p + 2\varepsilon_0 w_b, \quad (15)$$

where $\langle w \rangle$ is the average interstitial electrolyte velocity. Eq. (15) clearly shows buoyancy assisting pressure driven flow and the effect of the liquid fraction through $1 - 2\varepsilon_0$.

Electrode surface gas fraction

The gas fraction at the electrode surface, ε_0 , is hard to measure experimentally but is an important quantity. In this section, we provide an analytical model to estimate it. The average superficial gas velocity $\langle W_{g,c} \rangle$ due to gas generated at the cathode is related to the superficial gas velocity $U_{g,c}$ in the x -direction by the continuity equation as

$$\langle W_{g,c} \rangle = \int_0^z U_{g,c} dz / l = \frac{j' r_m z}{2Fl}, \quad (16)$$

where in the final expression, we assumed a constant current density j . The interstitial liquid velocity is related to superficial gas velocity $\langle W_{g,c} \rangle$ as

$$\langle W_{g,c} \rangle = \langle \varepsilon_c (w + w_s) \rangle, \quad (17)$$

where w_s is the vertical component of the slip velocity and only the cathodic part of the gas fraction is used. Usually, it can be neglected. However, we here provide expressions for electrode surface gas fraction assuming a constant slip velocity. It should be noted that the numerical solution includes all the slip velocities mentioned in Eq. (4). A similar expression can be derived for the superficial gas velocity $\langle W_{g,a} \rangle$ at the anode. For $\bar{\delta} \gg 1$, we can rewrite Eq. (17) as

$$\langle W_{g,c} \rangle = 2w_b \varepsilon_0^2 + (w_p + w_s) \varepsilon_0, \quad (18)$$

which on solving for ε_0 gives

$$\varepsilon_0 = \frac{\varepsilon_h^2}{2\varepsilon_l} \left(\sqrt{1 + \left(\frac{2\varepsilon_l}{\varepsilon_h} \right)^2} - 1 \right), \quad (19)$$

with $\varepsilon_l = \frac{\langle W_{g,c} \rangle}{w_p + w_s}$ and $\varepsilon_h = \sqrt{\frac{\langle W_{g,c} \rangle}{2w_b}}$, where ε_l and ε_h are the limiting expressions for ε_0 for low and high values, respectively. Eq. (19) can also be approximated by $\varepsilon_0 \approx (\varepsilon_l^p + \varepsilon_h^p)^{1/p}$ with a relative maximum error of less than 4% for $p = -1.43$ or about 20% for $p = -1$. This form manifestly shows that it is the smaller one of ε_l and ε_h that primarily determines ε_0 . Using Eq. (12), we can rewrite Eq. (17) for thin plumes ($e^{-1/\bar{\delta}} \ll 1$) with respect to interelectrode gap and small reduced pressure gradient as

$$\langle W_{g,c} \rangle = 6\bar{\delta}^3 w_b \varepsilon_0^2 + (6\bar{\delta} w_p (1 - 2\bar{\delta}) + w_s) \bar{\delta} \varepsilon_0, \quad (20)$$

and solve Eq. (20) using Eq. (14) for ε_0 to give Eq. (19), now with

$$\begin{aligned} \varepsilon_l &= \frac{\langle W_{g,c} \rangle}{\bar{\delta} (6\bar{\delta} \langle W \rangle (1 - 2\bar{\delta}) + w_s)}, \quad \varepsilon_h \\ &= \sqrt{\frac{\langle W_{g,c} \rangle}{6w_b \bar{\delta}^3 (1 - 12\bar{\delta} (1 - 2\bar{\delta}))}}. \end{aligned} \quad (21)$$

There are very few wall gas fraction measurements. Fukunaka et al., 1989 calculated the gas fraction using image analysis and Eq. (17) for low current density and low height to give $\varepsilon_0 \propto j^{1/2}$ and $\bar{\delta} \propto j^{0.26}$. At low current densities and low heights, it is expected that ε_l dominates. We note that $\langle W_{g,c} \rangle$ varies linearly with current den-

sity as given by Eq. (16). Using $\bar{\delta} \propto j^{0.26}$ in the expression for ε_l and neglecting the slip velocity in Eq. (21) gives $\varepsilon_0 \propto j^{0.48}$ similar to Fukunaka et al., 1989.

For higher heights, $\varepsilon_0 \approx \varepsilon_h$. Fukunaka et al., 1989 measured the average gas fraction in a bubble dispersion layer, proportional to ε_0 , to scale as $z^{0.26}$ and the plume thickness as $z^{0.31}$ for current densities above 93 A/m². We may approximate $(1 - 12\bar{\delta}(1 - 2\bar{\delta}))^2 \approx 6.5 \times 10^{-3} \bar{\delta}^{-1.5}$ as a power law in Eq. (21) for $0.06 < \bar{\delta} < 0.15$, so that with $\bar{\delta} \propto z^{0.31}$, ε_0 becomes proportional to $z^{0.27}$ very close to the scaling of gas fraction found by Fukunaka et al., 1989.

Pressure Drop

The scalings discussed at the end of the previous section, show that the wall gas fraction increases only weakly with height beyond a certain height. Assuming now a constant ε_0 , we can write the total pressure drop across the electrode height, $\Delta P \equiv P(h) - P(0) = -\frac{12\mu}{l^2} \int_0^h w_p dz$ by inserting w_p from Eq. (14) and $\bar{\delta} = \mathcal{A} z^a / \langle W \rangle^b$ as

$$\Delta P = -\frac{12\mu h \langle W \rangle}{l^2} \left(1 - \left(\frac{\langle W \rangle_{nc}}{\langle W \rangle} \right)^{1+2b} \left(1 - 2\bar{\delta}_h \frac{2a+1}{3a+1} \right) \right). \quad (22)$$

where $\bar{\delta}_h = \bar{\delta}|_{z=h}$. In the limit, $\varepsilon_0 \rightarrow 0$, Eq. (22) reduces again to the familiar Hagen–Poiseuille relation. The negative sign in front of $\langle W \rangle_{nc}$ shows that buoyancy opposes the pressure drop due to viscous friction. The velocity obtained for $\Delta P = 0$ in the limit $\bar{\delta} \ll 1$ is given by $\langle W \rangle = \langle W \rangle_{nc}$ where

$$\langle W \rangle_{nc} = \left(\frac{12w_b \varepsilon_0 (\mathcal{A} h^a)^2}{1 + 2a} \right)^{\frac{1}{1+2b}} \quad (23)$$

The subscript ‘nc’ stands for natural convection. Here, $\langle W \rangle_{nc}$ is the expected superficial velocity in case friction can be neglected for the natural convection flow. This may be a good approximation in the case of electrodes immersed in a large container.

Eq. (23) gives the upper limit for the natural convection velocity because at high velocity, dynamic pressure losses can not be neglected so that $\Delta P > 0$. Eq. (23) gives $\langle W \rangle_{nc} \propto l^{-3/5}$ for $b = 1/3$ as both ε_l and ε_h are proportional to l when slip can be neglected. A similar dependence of recirculation velocity on gap width, $l^{-0.5} - l^{-0.65}$, is reported in Hine and Murakami, 1980. We will use Eq. (23) in Section 5 to calculate the maximum height for a buoyancy driven electrolyzer.

Wall shear stress

Assuming a constant ε_0 , we can integrate Eq. (11) for thin plumes over the interelectrode gap to give the combined wall shear stress at a particular height z as

$$\tau_w = 2\mu \frac{\partial w}{\partial x} \Big|_{x=0} = \frac{12\mu}{l} (w_p + 2w_b \varepsilon_0 \bar{\delta}). \quad (24)$$

For single phase flow, the shear stress is given by $\tau_0 = 12\mu \langle W \rangle / l$. Therefore, we can write the ratio of the multiphase shear stress and single phase shear stress using Eq. (14) and Eq. (24) as

$$\frac{\tau_w}{\tau_0} = 1 + \frac{w_b \varepsilon_0 \bar{\delta} (2 - 12\bar{\delta} (1 - 2\bar{\delta}))}{\langle W \rangle}. \quad (25)$$

For thick plumes, integrating Eq. (11) gives the ratio $\frac{\tau_w}{\tau_0} = \frac{1}{1-2\varepsilon_0}$. Here, $1 - 2\varepsilon_0$ is the correction for increased interstitial velocity in the presence of average gas fraction $2\varepsilon_0$. Various authors have previ-

ously studied the pressure drop or shear stress multiplier, defined as the ratio of multiphase shear stress to single phase shear stress (Vogt, 1982; Thorpe et al., 1970; Hine et al., 1984; Clark and Flemmer, 1985; Nakoryakov et al., 1981). Eq. (25) shows that for forced flow assisting buoyancy, as considered here, the multiphase shear stress is always larger than the single phase shear stress for equal superficial liquid velocity. The multiphase shear stress increases as the average gas fraction increases, but decreases as the plume thickness increases. It should be noted that the wall shear stress in Eq. (24) and Eq. (25) varies with height z .

Validation and Discussions

In the first part of this section, we compare our numerical model with two different experimental measurements: one under forced flow conditions by Pang et al. (2020) and another under bubble-induced free convection by Boissonneau and Byrne (2000). Pang et al. (2020) estimated the gas fraction from images in the region above the electrodes, while Boissonneau and Byrne (2000) measured the velocity profiles in the inter-electrode gap of a small electrolyzer using laser doppler velocimetry (LDV). The dimensions and operating conditions for the experiments are listed in Table 1. In the second part of this section, we validate our analytical expressions for the surface gas fraction and velocity profile. In the third part, we verify the analytical pressure drop relation of Eq. (22) against the numerical simulations.

Validation of Numerical Model

We solved the mixture model formulation in COMSOL v5.6, as described in Section 2.2. At the top, an outlet boundary condition is used with a pressure of 0 Pa so that both the gas and the liquid can flow out of the domain. A parabolic velocity inlet boundary condition is used at the bottom of the channel with zero gas flux such that the average velocity just below the electrode matches the average velocity measured in the experiments, as shown in Fig. 2. This means that the flow enters the electrode as fully developed, which may not be true if the velocity is high. However, for the conditions of Boissonneau and Byrne, 2000, $h_{\text{en}} = 40$ mm is approximately equal to the entrance length for a laminar flow (Atkinson et al., 1969), $(0.625 + 0.044\text{Re})l \approx 34$ mm, at the maximum velocity $\langle W \rangle = 0.08$ m/s observed at 2000 A/m². Therefore, we can expect the flow to be parabolic at the bottom of the electrode for the conditions of Boissonneau and Byrne, 2000. At the electrode wall, we assume a constant current density and associated superficial gas velocity given by Eq. (5). In our simulations,

Table 1
Dimensions and operating conditions for validation cases

Properties	Pang et al. (2020)	Boissonneau and Byrne (2000)
Electrode	2 nm Ti and 50 nm Pt deposited sequentially on Ti foil substrate	coated Titanium at Cathode and DSA [®] at Anode
Electrolyte	0.5 M H ₂ SO ₄	50 g/l Na ₂ SO ₄ (or 0.35 M)
Inter-electrode gap, l	4 mm	3 mm
Electrode height, h	9 mm	40 mm
Channel height above electrode, h_{exit}	12 mm	40 mm
Channel height below electrode, h_{en}	95 mm	40 mm
Temperature, T	60° C	25° C
Pressure	1 atm	1 atm
Electrolyte density, ρ	1030 kg/m ³	1040 kg/m ³
Electrolyte viscosity, μ	1.1 mPa-s	1.03 mPa-s

we use a constant bubble diameter at a given current density, see Table 2. Boissonneau and Byrne (2000) measured up to two times larger average hydrogen bubble diameter at the top compared to the bottom of the electrode. We used the average bubble diameter measured at the top of the electrode, as listed in Table 2. The bubble diameter is assumed to be the same for both hydrogen and oxygen, as no information about the size of oxygen bubbles was provided in the two references.

Fig. 3 shows the liquid velocity vector overlaid on the contour plot of gas fraction. We see that the gas moves in a plume near the electrode surface and the gas fraction increases along the height of the electrode. The liquid velocity is initially parabolic at the bottom of the electrode, but changes its shape due to buoyancy of the bubbles.

Fig. 4 shows the magnitude of slip velocity near the top of the electrode ($z = 35$ mm) for the validation case solved in COMSOL corresponding to the experiments of Boissonneau and Byrne (2000) at 2000 A/m². The properties are listed in Table 1 and Table 2. It can be seen that the slip velocity due to hydrodynamic diffusion, Saffman force and shear-induced diffusion are important, while shear migration can be neglected both in horizontal and vertical direction. The hydrodynamic diffusion slip velocity is larger where the gas fraction is smaller. This is because the hindrance factor $f(\varepsilon)$ reduces its magnitude in the region of high gas fraction and this slip velocity is inversely proportional to the gas fraction. The horizontal slip velocity due to Saffman force and shear-induced diffusion is significant near the electrodes due to high shear rate in these regions.

Plume Thickness

Here, we compare the plume thickness along the height h_{exit} above the electrode with the experimental data from Pang et al. (2020). Fig. 5 shows the contour lines corresponding to the location where 99% and 60% of the gas is located inside the plume for the two different Reynolds numbers. We see a good agreement between the numerical model and the experimental measurements. The analytical expression of Eq. (8) is also shown in Fig. 5. In order to find the most suitable values of \mathcal{A} , a , and b , we performed multiple simulations for the configuration used by Boissonneau and Byrne (2000) for current densities of 500 A/m², 1000 A/m² and 2000 A/m² at different forced flow conditions such that $\langle W \rangle$ ranges between 0.06 m/s and 0.33 m/s. Using the data from the simulations, we obtained the e-folding plume thickness δ at every 1 mm between $h = 0$ mm and $h = 40$ mm by fitting

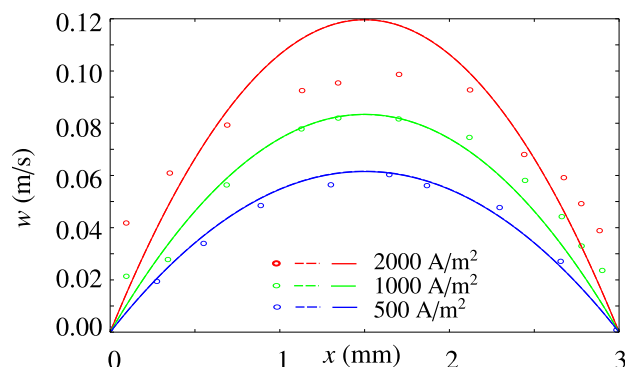


Fig. 2. Velocity profiles at $z = -5$ mm slightly below the electrode (see Fig. 1), for the three current densities: $j = 2000$ A/m² (red), $j = 1000$ A/m² (green) and $j = 500$ A/m² (blue). The circles represent the experimental measurements from Boissonneau and Byrne (2000), the dashed line represents the numerical solution and the almost overlapping solid line represents the approximate analytical solution of Eq. (A.2). The parameters used are listed in Table 1, Table 2 and Table 3 for buoyancy driven conditions. Eq. (A.2) gives a parabola when $\varepsilon_0 = 0$.

Table 2

Average hydrogen bubble diameter measured experimentally at the top of the electrode for different validation cases. The Reynolds number is defined as $Re = \rho ul / \mu$.

Validation Case	d_b [μm]	$\langle W \rangle_{in}$ [m/s]
Forced Flow (Pang et al. (2020))		
$j = 2000 \text{ A/m}^2$, $Re = 297$	157	0.08
$j = 2000 \text{ A/m}^2$, $Re = 796$	150	0.214
Natural Recirculation (Boissonneau and Byrne (2000))		
$j = 500 \text{ A/m}^2$	62	0.041
$j = 1000 \text{ A/m}^2$	74	0.056
$j = 2000 \text{ A/m}^2$	87	0.08

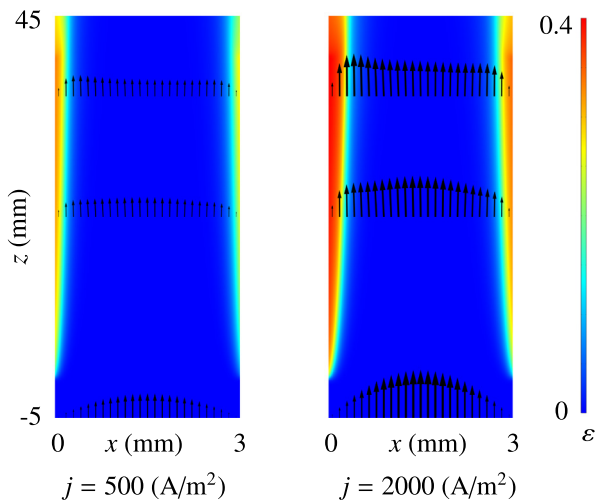


Fig. 3. Liquid velocity vectors overlaid on contour plots for gas fraction. The size of the arrow vector represents the magnitude of the velocity. The parameters used are listed in Table 1, Table 2 and Table 3 for buoyancy driven conditions. The velocity vectors are shown at $z = -5 \text{ mm}$, $z = 20 \text{ m}$ and $z = 35 \text{ m}$. It can be seen that the velocity is initially parabolic as shown in Fig. 2, but changes its shape along the vertical coordinate as the gas fraction increases.

Eq. (6) such that the average gas fraction (ε) and the electrode gas fraction ε_0 are the same as in the numerical solution. Using this plume thickness data, we performed regression using the least squares method to obtain the values of \mathcal{A} , a and b reported in Table 3. It can be seen from Fig. 7 that the estimated parameter values give a reasonable fit for the simulated plume thickness. We also note from Table 3 that \mathcal{A} varies with current density. Since, in our model, current density is proportional to volumetric flux $U_{g,c}$ from Eq. (5), we write, for forced flow

$$\mathcal{A} \approx 4.4 \times 10^{-2} \sqrt{U_{g,c}}, \quad (26)$$

as shown in Fig. 6. Eq. (26) should be used with caution, as it is obtained for forced flow conditions for only three data points. The effect of experimentally observed increased bubble diameter with increasing current density is included in Eq. (26). Pang et al., 2020 also found a similar power of $j^{0.47}$ for forced flow conditions, however Bongenaar-Schlechter et al., 1985 observed a much smaller power of $j^{0.1}$.

In our simulations, we used the bubble sizes in Table 2, independent of velocity. Higher velocities result in smaller bubbles (Pang et al., 2020; Eigeldinger and Vogt, 2000; Landolt et al., 1970). In addition to the direct effect of flow on the plume width, this further reduces the plume thickness. This is because a decrease in bubble size results in smaller lateral dispersion of bubbles as the slip velocities in the lateral direction are proportional to d_b , see Eq. (4). As such, the numerically obtained value of b may be an overestimation. Referring to Fig. 9, we solve Eq. (A.4) and Eq. (A.8), using Table 1 and Table 3, simultaneously to obtain the wall gas fraction.

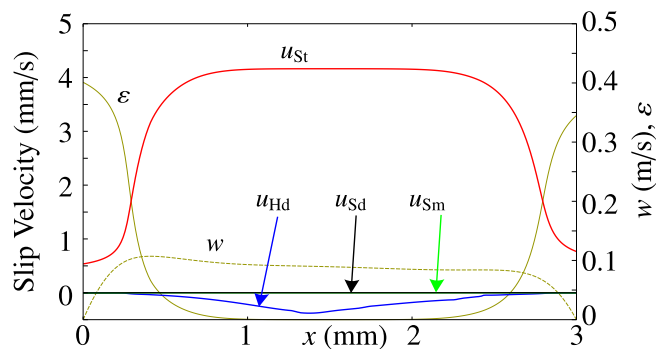
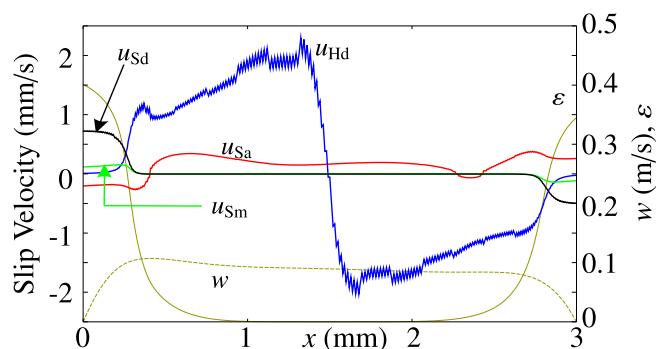
(a) Vertical slip velocities at $z = 35 \text{ mm}$ **(b) Horizontal slip velocities at $z = 35 \text{ mm}$** 

Fig. 4. Magnitude of slip velocities near the top of the electrode ($z = 35 \text{ mm}$) for the validation case corresponding to the experiments of Boissonneau and Byrne (2000) at 2000 A/m^2 . The top figure shows the vertical slip velocities. It can be seen that in the vertical direction, the Stokes slip velocity due to buoyancy is dominant, while the shear migration and shear diffusion slip velocities are negligible. In the horizontal direction, the shear migration slip velocity is always negligible compared to other slip velocities. The slip velocities due to Saffman lift force and shear-induced diffusion are dominant near the wall, while hydrodynamic diffusion becomes important in the bulk region where the gas fraction gradient is large and gas fraction is small.

Using the obtained wall gas fraction, we use Eq. (A.1) to plot gas fraction profile. we note that the plumes are not exactly exponential, especially at higher heights and current densities. Therefore, we expect deviations from our analytical model, particularly for these conditions.

Velocity Profile

In Fig. 10, we compare the velocity profiles from the numerical model against the experiments from Boissonneau and Byrne (2000) at different electrode heights and current densities. The model shows good agreement with the experimental data. The simplification of assuming a constant diameter in the numerical model is a likely reason for small discrepancies. It should be noted that the measured velocities in Fig. 10 are always higher than the velocities from the numerical and semi-analytical model. In part, this is because laser doppler velocimetry measures the bubble velocity, which is always slightly higher than the liquid velocity due to slip. For a bubble diameter of $88 \mu\text{m}$, we can estimate w_{st} to be approximately 4 mm/s , see also Figure 4. The oxygen bubbles may be larger, giving larger slip velocities – see Appendix D.

Validation of Analytical Model

Gas fraction at the electrode

For the experimental values of $\langle W \rangle$ from Boissonneau and Byrne (2000), we solve Eq. (A.4) and Eq. (A.8) numerically to get the gas fraction ε_0 and w_p at a certain height. Since different amount of gas

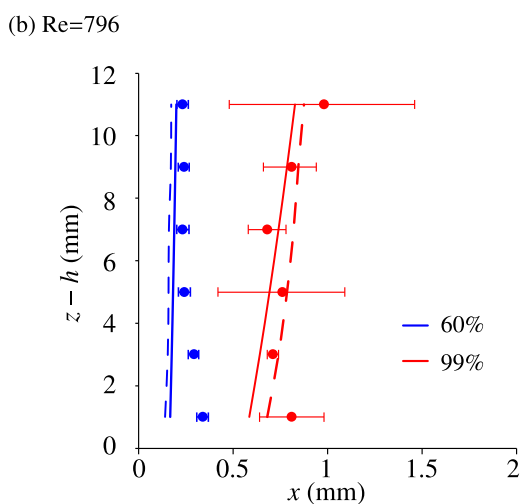
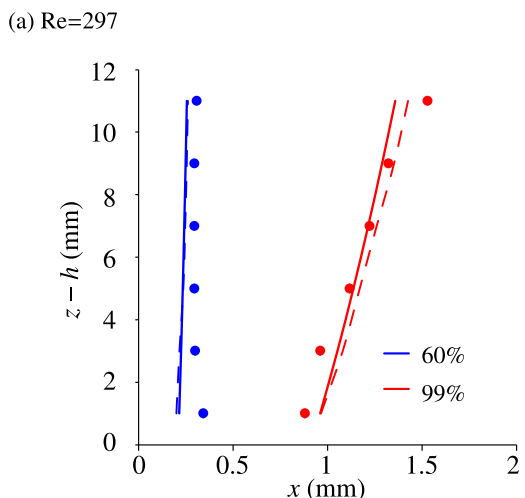


Fig. 5. Contour lines corresponding to the locations where 60% and 99% of the hydrogen gas is located within the plume. The circles with error bars represent the experimental measurements from Pang et al. (2020) and the dashed line represents our numerical solution. The solid line represents the profile using Eq. (8) with $a = 0.5, b = 0.33$ and $\mathcal{A} = 8.4 \times 10^{-4} \text{ m}^{0.83}/\text{s}^{0.33}$ for the 60% profile. For the 99% profile, we used $\mathcal{A} = 2.1 \times 10^{-3} \text{ m}^{0.83}/\text{s}^{0.33}$.

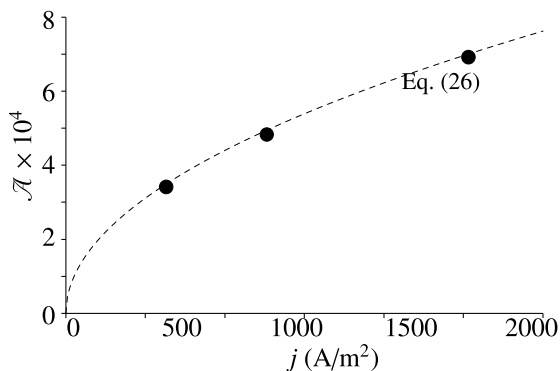


Fig. 6. Variation of \mathcal{A} with volumetric gas flux in horizontal direction $U_{g,c}$ for forced flow simulations corresponding to the configuration used by Boissonneau and Byrne (2000). We see that \mathcal{A} , shown as solid circles, varies roughly as the square root of volumetric flux given by Eq. (26) for these simulations. It should be noted that the current density is proportional to volumetric flux according to Eq. (5).

Table 3

Estimated parameters for plume thickness using a least square fit on simulation results for the configuration used by Boissonneau and Byrne (2000). While the electrolyzer used in Boissonneau and Byrne, 2000 operates using buoyancy driven flow, the forced flow results are obtained by doing multiple numerical simulations with different inlet velocities. The power of $b = 1/3$ is also observed by Schillings et al. (2015) and follows from theoretical scaling arguments.

At buoyancy-driven conditions (Boissonneau and Byrne, 2000)			
j (A/m ²)	a	$\mathcal{A}/(W)^b$	
500	0.35	6.6×10^{-4}	
1000	0.39	9.2×10^{-4}	
2000	0.4	1.2×10^{-3}	
Forced flow			
j (A/m ²)	a	b	\mathcal{A}
500	0.44	0.33	3.4×10^{-4}
1000	0.45	0.33	5×10^{-4}
2000	0.45	0.32	6.9×10^{-4}

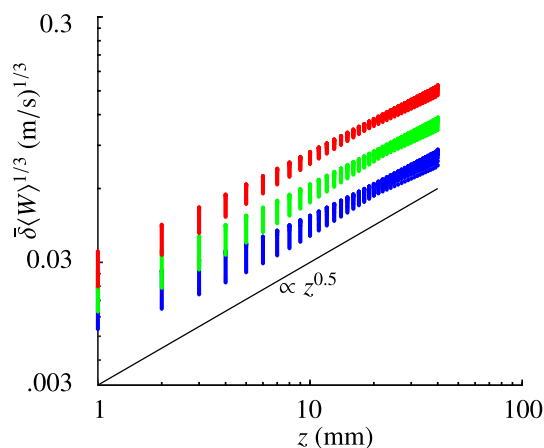


Fig. 7. Scatter plot for simulated e-folding plume thickness δ for different heights, inlet velocities and current densities for the configuration of Boissonneau and Byrne (2000) and corresponding properties listed in Table 1. The plot contains data from 40 different heights ranging from 1 mm to 40 mm at different forced flow conditions, such that (W) ranges between 0.06 m/s and 0.33 m/s. The blue, green and red dots corresponds to $j = 500 \text{ A/m}^2, j = 1000 \text{ A/m}^2$ and $j = 2000 \text{ A/m}^2$, respectively. It can be seen that the plume thickness can be approximated reasonably well with $\frac{\mathcal{A}z}{(W)^b}$ over this range of parameters where \mathcal{A}, a and b are listed in Table 3.

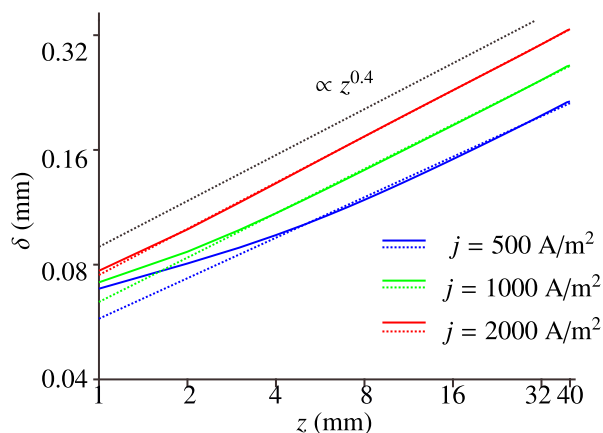


Fig. 8. Log-log plot for e-folding plume thickness δ with height z obtained from our numerical model for the buoyancy driven flow in the configuration used by Boissonneau and Byrne (2000). The colored dotted lines represent the power law relation fitted using regression with parameters listed in Table 3. The black dotted line indicates a slope of 0.4. It can be seen that at low values of δ , the power law underestimates the plume thickness.

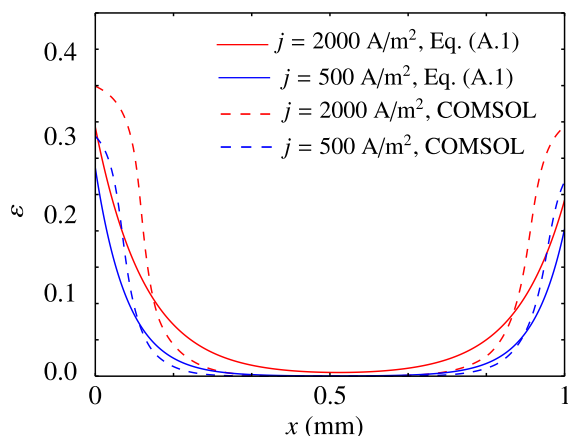


Fig. 9. Gas fraction profiles for the configuration used by Boissonneau and Byrne (2000). COMSOL simulation results are compared with the solution of Eq. (A.1), using Eqs. (A.4) and Eq. (A.8) and Table 1 and Table 3 to determine the wall gas fraction. It can be seen that at low current density, the gas fraction varies approximately exponentially with x while at larger current densities, the gas fraction profiles are not exponential. Due to this, the estimated e-folding plume thickness using the procedure described in Section 3.2 overestimates the growth of plume thickness with height. This deviation from an exponential profile will result in errors at higher heights and larger current densities.

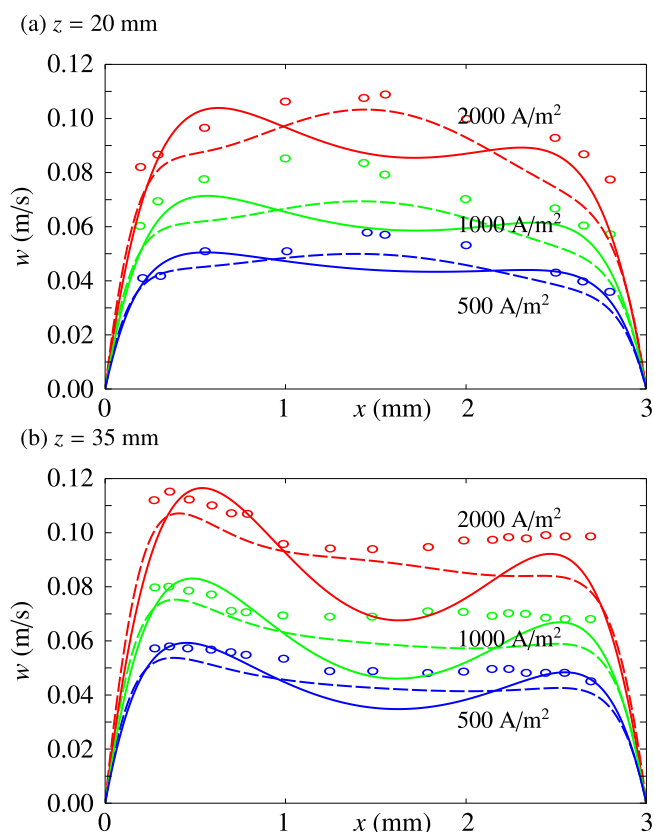


Fig. 10. Velocity profiles for the three current densities: $j = 500 \text{ A/m}^2$ (blue), $j = 1000 \text{ A/m}^2$ (green), and $j = 2000 \text{ A/m}^2$ (red). The circles represent the experimental measurements from Boissonneau and Byrne (2000), the dashed line represents the numerical solution and the solid line represents the semi-analytical solution. Here, we used Eq. (A.2) to capture the asymmetry between anode and cathode for water electrolysis. For δ , we used parameters in Fig. 8. It should be noted that the experimental velocity profiles are measured using laser Doppler velocimetry, and hence represent bubble velocities. The liquid velocities are slightly lower than the bubble velocities due to the slip velocity.

is generated at the cathode and the anode as described by Eq. (5), we use an anode wall gas fraction that is $Q = 0.8$ times that at the cathode. In Fig. 11, we compare the analytical approximation for the cathode ε_0 with that of the numerical model. We see that the analytical model gives a similar trend for the gas fraction at the electrode surface as the numerical model. Compared to the numerical model, the analytical gas fraction is lower, especially at larger heights. This is because we neglected the effect of inertial terms in our analysis. As such, the analytical profiles have a larger peak velocity (see Fig. 10). From Eq. (17), this gives a lower gas fraction.

Velocity profile

For calculating the analytical velocity profile, we use the semi-analytical values of ε_0 and w_p obtained in the previous section at a particular height to plot the velocity profile in Fig. 10 using Eq. (A.2). Here, we used the relations from the appendix to reproduce asymmetric profiles due to different wall gas fractions at the two electrodes. We see a reasonable agreement of the semi-analytical model with the numerical model and experimental measurements. The analytical results do not show the small velocity peak in the center of the channel that is visible from simulations at $z = 20 \text{ mm}$ and $j = 1000 \text{ A/m}^2$ and $j = 2000 \text{ A/m}^2$. The analytical results also show a higher velocity peak near the electrode surface. The

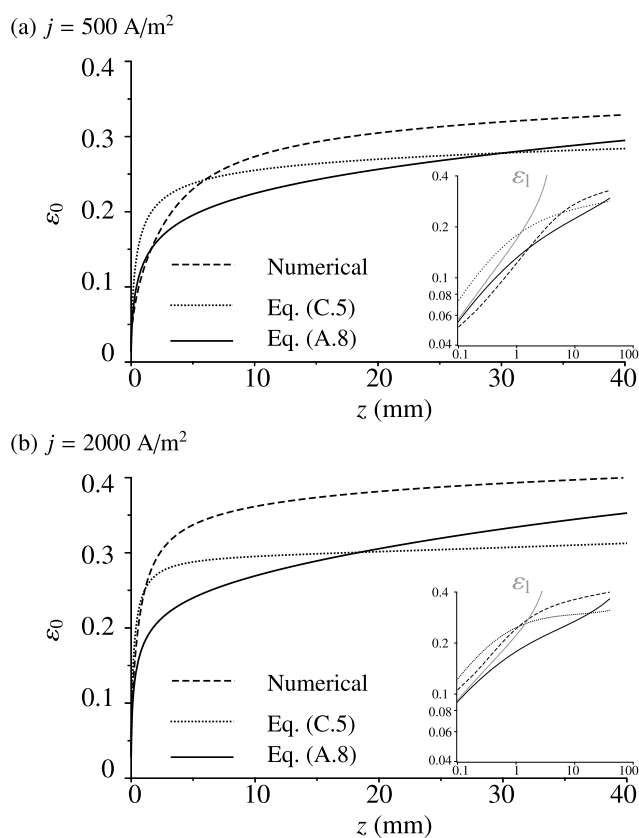


Fig. 11. Variation of gas fraction at the cathode surface, ε_0 with the vertical z -coordinate, z at different current densities. The solid line represents the semi-analytical solution of Eq. (A.8), the dotted line represents the semi-analytical solution for a constant gas fraction plume given by Eq. (C.5) using the values listed in Table 3 for the buoyancy driven conditions, and the dashed line represents the solution from the numerical model. We neglected the inertial term in our semi-analytical solution giving a larger peak velocity than that obtained using COMSOL as shown in Fig. 10. Because most of the gas is localized near the electrode surface, the larger velocity results in lower gas fraction according to mass conservation (see Eq. (17)). A log-log plot is shown in the inset. The solid gray line represents the solution for small gas fraction given by Eq. (A.9). From Eq. (A.9), $\varepsilon_1 \propto z^{1-2a}$, which gives $z^{0.3}$ for $j = 500 \text{ A/m}^2$ and $z^{0.2}$ for $j = 2000 \text{ A/m}^2$ using the value of 'a' at buoyancy driven conditions in Table 3.

discrepancy arises because we neglected the inertial term, which lowers the velocity near the peak and increase the velocity in the bulk. At higher current densities, the deviation from the numerical model is larger because our assumption of thin exponential plumes no longer holds.

Pressure Difference

Due to lack of experimental data, we rely on our validated numerical simulations to verify Eq. (22) for the pressure drop along the electrode height. We used the configuration from [Boissonneau and Byrne \(2000\)](#) and carried out various numerical simulations under forced flow conditions for $j = 1000 \text{ A/m}^2$ by varying the inlet velocities. Fig. 12 shows the variation of the reduced pressure difference, ΔP with the superficial velocity, $\langle W \rangle$. The analytical pressure drop shows a reasonable agreement with the numerical results. At low velocities, the presence of gas makes the reduced pressure drop positive, as the effect of buoyancy becomes larger than that of friction. At high velocity, the plumes become thinner, while the viscous forces are increased due to the modified viscosity $\frac{\mu}{1-\varepsilon_0}$. Due to this increase, the total pressure drop becomes similar to that for a single phase flow. We neglected the inertial term in our model, which results in large deviation, particularly, at high velocities. At low velocities, buoyancy is dominant and the error due to inertial terms is small. The deviation at low velocities is primarily because the plume thickness becomes large, and our assumption $\bar{\delta} \ll 1$ is only crudely satisfied.

Design Guidance

We can use our analytical model to guide the design of membraneless parallel plate electrolyzers. To avoid bubble crossover, thick plumes are not desired. To avoid mixing of hydrogen and oxygen, at the top of the electrode, a divider to separate the gases should be present. For safe operation of electrolyzer, the amount of H_2 should not exceed the lower explosion limit of 4% in O_2 . Since twice as much hydrogen volume is produced compared to oxygen, this requires the cross-over rate of hydrogen to stay below 2%. We will assume that at least 98% of the gas fraction is contained between $x = 0$ and $x = l/2$,

$$\frac{\int_0^{l/2} \varepsilon_0 e^{-x/\delta} dx}{\int_0^l \varepsilon_0 e^{-x/\delta} dx} = \frac{1}{e^{-l/2\delta} + 1} > 0.98. \quad (27)$$

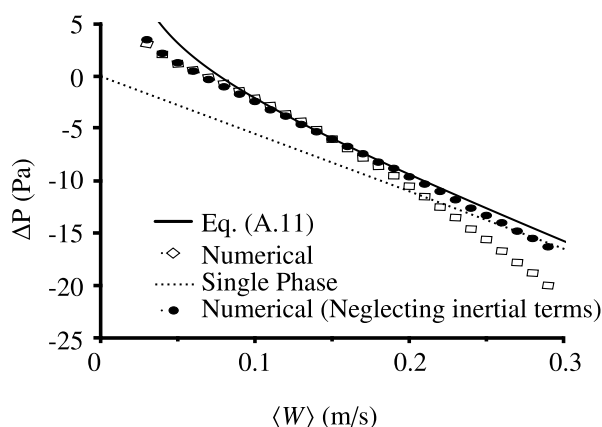


Fig. 12. The predicted reduced pressure difference between the top and the bottom of the electrode plotted against the superficial velocity for $h = 40 \text{ mm}$. The configuration used is similar to that used by [Boissonneau and Byrne \(2000\)](#), see [Table 1](#). The hollow diamonds represent results from numerical simulations, the black dots represent the numerical solution neglecting the inertial terms, the solid black line represents the result from Eq. (A.11) and the dotted line represents the Hagen-Poiseuille pressure drop.

It would be more accurate to multiply the integrands with the gas velocity $u + w_s$. However, to obtain more transparent expressions, we here take this simpler approach. Solving for l gives

$$l \gtrsim 7.8 \delta_h = 7.8 \frac{\mathcal{A} h^a}{\langle W \rangle^b}. \quad (28)$$

From Eq. (28), requiring the gap to be almost an order of magnitude larger than the plume thickness may seem like a very conservative criterion. However, mind that our δ is that distance after which the gas fraction has decreased to a fraction $1/e = 0.37$ of its value at the electrode. Plume thickness decreases with an increase in vertical velocity of the electrolyte for a laminar flow. However, at large velocities, the flow may become turbulent leading to a thicker plume ([Pang et al., 2020](#)). Therefore, the maximum velocity is limited by transition to turbulence. We can rearrange Eq. (28) using $\langle W \rangle = \frac{\text{Re}\mu}{\rho l}$, to give

$$h \lesssim \left(\frac{\langle W \rangle^b l}{7.8 \mathcal{A}} \right)^{1/a} = \left(\frac{l^{1-b} (\text{Re}\mu)^b}{7.8 \mathcal{A} \rho} \right)^{1/a}. \quad (29)$$

Using Eq. (26) with properties from [Table 1](#) and [Table 3](#), corresponding to [Boissonneau and Byrne, 2000](#), we can express Eq. (29) as

$$h \lesssim 10.8 \frac{\langle W \rangle^{0.7} l^{2.2}}{U_{g,c}^{1.1}}. \quad (30)$$

We again note that the power 0.5 in Eq. (26) is obtained using forced flow simulations for the configuration used by [Boissonneau and Byrne \(2000\)](#), and a more detailed analysis of how the plume thickness varies with current density is warranted. Therefore, Eq. (30) should be treated as a tentative result. Eq. (29) and Eq. (30) shows that a larger interelectrode gap l allows a larger electrode height without significant gas crossover. However, this also increases the ohmic losses. Therefore, the maximum possible electrode height will be limited by the maximum allowable ohmic losses.

We also note that the maximum height increases with decrease in volumetric flux of the gas in the horizontal direction. In [Fig. 13](#), we see that for a lower current density, the maximum height of the electrolyzer increases because a smaller current density corresponds to a lower horizontal volumetric flux of the gas. Similarly, a higher pressure decreases the molar volume of the gas, thereby decreasing the volumetric flux. As such, operation at higher pressure will give a larger maximum height for the electrolyzer.

In order to see whether parallel plate electrolyzers without separators can be a viable alternative to electrolyzers with separators, we provide design estimates so that the ohmic losses are lower than those of zero-gap electrolyzers with modern separators. The most commonly used Zirfon Perl diaphragm has a thickness of only 0.5 mm, but the ohmic losses are usually equivalent to 3.3 mm – 5 mm of KOH in a zero-gap configuration due to geometrical and gas effects ([Haverkort and Rajaei, 2021](#); [de Groot and Vreman, 2021](#)). Therefore, we consider a membraneless parallel plate electrolyzer of 3 mm, giving lower ohmic losses than a zero-gap electrolyzer with Zirfon Perl separator. There will also be additional ohmic losses due to bubbles, but the multiplier ($\approx \int_0^1 (1-\varepsilon)^{-3/2} d\bar{x}$) using Bruggeman's relation ([Bruggeman, 1935](#)) will be close to 1 for thin plumes.

We first consider the design of the buoyancy driven electrolyzer used by [Boissonneau and Byrne \(2000\)](#). Inserting $\langle W \rangle_{nc}$ from Eq. (A.12) in Eq. (28) gives

$$h_{\max} \approx \left(\frac{l}{\mathcal{A}} \left(\frac{6w_b \varepsilon_0 (2 - \varepsilon_0 + k_2/2)}{7.8 \frac{1-2b}{b} (1+2a) (1 + \frac{6\varepsilon_0 \rho_{\max}}{1+a})} \right)^b \right)^{\frac{1}{a}}. \quad (31)$$

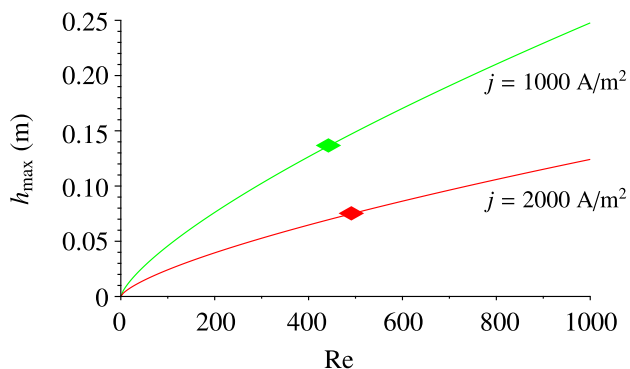


Fig. 13. Maximum height h_{\max} as a function of Reynolds number for a gap width of 3 mm at atmospheric pressure. The buoyancy driven conditions are represented by the filled diamond. It can be seen that an increase in Reynolds number significantly increases the maximum allowable height of the membraneless parallel plate electrolyzer. The properties used are listed in Table 1 and Table 3.

where $\bar{\delta}_{\max} \approx 1/7.8$ is the maximum allowable dimensionless plume thickness given by Eq. (27) and k_2 is defined in Appendix A. For equal gas fraction at both electrodes, $k_2 = 0$. Using Eq. (31) and values from Table 3, we find that $h_{\max} \approx 13.6$ cm for $l = 3$ mm at 1000 A/m^2 , assuming $\varepsilon_0 = 0.3$, and $h_{\max} \approx 7.5$ cm at 2000 A/m^2 , assuming $\varepsilon_0 = 0.35$. These are the upper limits because Eq. (A.12) overpredicts the natural recirculation velocity. Friction in the external hydraulic circuit, including the downcomer is not taken into account. Also, at high velocities dynamic pressure losses will be important, and therefore the actual recirculation velocity will be smaller, giving a smaller height.

We can also increase the liquid velocity to increase the height of the electrolyzer as shown in Fig. 13. However, very high velocities can give rise to turbulence that enhances mixing, giving thicker plumes. This has been experimentally observed by Pang et al. (2020) where turbulence starts increasing the plume thickness at a Reynolds number, $Re \gtrsim 1200$. At $Re = 1000$, Eq. 29, using the values in Table 3 from Boissonneau and Byrne (2000), gives the maximum electrode height h_{\max} without significant crossover as 24.8 cm and 12.4 cm for a current density of 1000 A/m^2 and 2000 A/m^2 , respectively. This shows that using forced flow, the electrode height can be increased by more than two times.

For the electrode used by Pang et al. (2020), the fit of Fig. 5 gives for $j = 2000 \text{ A/cm}^2$, a slightly larger plume thickness than in the configuration used by Boissonneau and Byrne (2000). This may be attributed to the larger bubble size in the experiments by Pang et al. (2020) ($\sim 150 \mu\text{m}$) compared to those in the experiments of Boissonneau and Byrne (2000) ($\sim 88 \mu\text{m}$). The plume thickness crudely scales with $\delta \propto d_b^{2/3}$ observed by Schillings et al. (2015) at high current density, for which shear induced diffusion becomes dominant. Eq. 29, in this case, gives a maximum height of 10.6 cm at $Re = 1000$ for $j = 2000 \text{ A/cm}^2$. It should be noted that the size of the electrode can still be increased by increasing the depth of the electrode to increase the total production rate. However, to further scale-up the height of the electrolyzer, the electrode should be designed such that the bubble size remains small. This can be done, for example, by using surfactants (Esposito et al., 2017; Angulo et al., 2020), using a more hydrophilic surface (Kim et al., 1947), engineering the topology of the electrode surface with micro-crevices (Groß et al., 2018), or using magnetic fields (Koza et al., 2011).

Conclusions

In this paper, we provided both numerical and analytical modeling approaches to study the multiphase flows in a membraneless

parallel plate electrolyzer. Our numerical model is based on a mixture model approach and is used to find the dependence of plume thickness on height, velocity and current density. Using the momentum equation and neglecting inertial terms, analytical relations for the interstitial velocity (Eq. (12)) and superficial velocity (Eq. (14)) in the interelectrode gap are derived and verified against the numerical model and existing experimental results. These expressions are valid as long as the plumes remain exponential and thin compared to the gap width. These assumptions will not hold above a certain height at high current densities and low velocities. We also derived an expression for the gas fraction at the electrode surface (Eq. (20)) using mass conservation and found that the gas fraction at the electrode increases rapidly in the first few millimeters of electrode height. Furthermore, we derived an analytical expression for the pressure drop along the electrode height (Eq. (22)). At high velocities, the pressure change due to buoyancy is approximately compensated by the increased viscosity and wall shear rate.

Finally, analytical expressions for maximum height (Eq. (29)) for safe operation of a membraneless parallel plate electrolyzer are provided for a given electrode gap. With the help of analytical results, we calculated this maximum height of the electrolyzer at buoyancy driven and forced flow conditions. We showed that the maximum height of the electrode decreases as the current density increases. We find that for an ohmic loss comparable to that of a zero-gap electrolyzer, we can design a membraneless parallel plate electrolyzer operating using natural recirculation with a maximum height of ~ 7 cm at atmospheric pressure and a current density of 2000 A/m^2 and a product purity of 98%. The maximum height of the electrolyzer scales with the inter-electrode gap width l roughly as $l^{1/a} \sim l^{2.2}$. Thus, a larger gap will allow a significantly taller electrolyzer using only buoyancy driven flow. While the transition to turbulence limits the potential of using forced flow somewhat, the maximum height of the electrolyzer can be significantly increased by using a forced flow, higher pressure, or smaller bubbles.

Declaration of Competing Interest

The authors declare that they have no known competing financial interests or personal relationships that could have appeared to influence the work reported in this paper.

Relations for different anode and cathode surface gas fraction to $\mu_m = \frac{\mu}{1-\varepsilon}$

In this section, we generalize the results of main text, valid for $\mu_m = \mu$, to $\mu_m = \frac{\mu}{1-\varepsilon}$ and different electrode surface gas fractions. We define Q as the ratio of the gas fraction at the anode surface and the gas fraction at the cathode surface and rewrite Eq. (6) for exponential plumes as

$$\varepsilon = \varepsilon_0 \left(e^{-\frac{x}{\delta}} + Q e^{-\frac{l-x}{\delta}} \right). \quad (\text{A.1})$$

Solving Eq. 11 using Eq. (A.1) with no-slip boundary conditions for thin plumes ($e^{-1/\delta} \ll 1$) we get

$$\begin{aligned} w &= 6w_p \bar{x} (k_1 - \bar{x}) + 12(w_p + w_b) \varepsilon_0 \delta^2 \left(1 - e^{-\frac{x}{\delta}} \right) \left(1 - Q e^{-\frac{l-x}{\delta}} \right) \\ &+ 6w_p \varepsilon_0 \delta \left(\left(e^{-\frac{x}{\delta}} - Q e^{-\frac{l-x}{\delta}} \right) (k_1 - 2\bar{x}) - k_1 \right) \\ &- 6w_b \varepsilon_0^2 \delta^2 \left(1 - e^{-\frac{2x}{\delta}} \right) \left(1 - Q^2 e^{-\frac{2(l-x)}{\delta}} \right) \\ &- 6w_b \varepsilon_0 \delta^2 k_2 \left(\varepsilon_0 \delta \left(e^{-\frac{x}{\delta}} - Q e^{-\frac{l-x}{\delta}} - 1 \right) + \bar{x} \right), \end{aligned} \quad (\text{A.2})$$

where $k_1 \equiv \frac{1-2\bar{\delta}\varepsilon_0(Q-(Q-1)\bar{\delta})}{1-\bar{\delta}\varepsilon_0(Q+1)}$ and $k_2 \equiv \frac{(Q-1)(2-(Q+1)\varepsilon_0)}{1-\bar{\delta}\varepsilon_0(Q+1)}$. For $Q < 2$, $\varepsilon_0 < 0.5$ and $\bar{\delta} < 0.5$, $k_1 \approx 1$ is a reasonable approximation. The shear rate at the cathode surface is given by

$$\left. \frac{\partial w}{\partial x} \right|_{x=0} = 6(1 - \varepsilon_0)(w_p k_1 + w_b \varepsilon_0 \bar{\delta}(2 + \bar{\delta}k_2)) \quad (\text{A.3})$$

The average superficial velocity, $\langle W \rangle = \int_0^1 w(1 - \varepsilon)d\bar{x}$ using Eq. (A.2) for $w_b \gg w_p$, can be written as

$$\begin{aligned} \langle W \rangle &= w_p \left(1 - 6\varepsilon_0 \bar{\delta}(1 - 2\bar{\delta}) \right) + 3w_b \varepsilon_0 \bar{\delta}^2 k_2 \left(1 - 2\bar{\delta} \varepsilon_0 (Q + 1) \right) \\ &\quad + 3w_b \varepsilon_0 \bar{\delta}^2 \left(4 - 2\varepsilon_0 - (4(Q + 1) + \varepsilon_0(1 - 3Q^2 + 4Q))\bar{\delta} \right). \end{aligned} \quad (\text{A.4})$$

For $Q = 1$, Eq. (A.4) reduces to

$$\langle W \rangle = w_p \left(1 - 6\varepsilon_0 \bar{\delta}(1 - 2\bar{\delta}) \right) + 12w_b \varepsilon_0 \bar{\delta}^2 \left(1 - 2\bar{\delta} - \frac{\varepsilon_0(1+\bar{\delta})}{2} \right). \quad (\text{A.5})$$

The differences with Eq. 13 are of the order ε_0 as expected. In the limit $\bar{\delta} \gg 1$, the velocity profile is given by

$$u = 6\bar{x}(1 - \bar{x})(w_p + w_b \varepsilon_0(Q + 1))(1 - (Q + 1)\varepsilon_0). \quad (\text{A.6})$$

The extra $(1 - (Q + 1)\varepsilon_0)$ term in Eq. (A.6) is due to $\mu_r = \frac{1}{1-\varepsilon}$, where the gas fraction becomes a constant given by $\varepsilon = (Q + 1)\varepsilon_0$. For $\bar{\delta} \gg 1$, the superficial velocity, $\langle W \rangle = \int_0^1 u(1 - \varepsilon)d\bar{x}$ can be written as

$$\langle W \rangle = (w_p + (Q + 1)w_b \varepsilon_0)(1 - (Q + 1)\varepsilon_0)^2. \quad (\text{A.7})$$

Here again, we see the combined effect of modified viscosity and the effect of liquid gas fraction on superficial velocity through the term $(1 - (Q + 1)\varepsilon_0)^2$ in a buoyancy assisted pressure driven flow.

Using Eq. (A.2), we can rewrite Eq. (17) for $e^{-1/\bar{\delta}} \ll 1$ as

$$\begin{aligned} \langle W_{g,c} \rangle &= -(3k_2 \bar{\delta} + 4)\bar{\delta}^3 w_b \varepsilon_0^3 + 3\bar{\delta}^2 (2w_b \bar{\delta}(1 + k_2 \bar{\delta}) - w_p(k_1 - \bar{\delta}))\varepsilon_0^2 \\ &\quad + 6w_p \bar{\delta}^2 \varepsilon_0(k_1 - 2\bar{\delta}) + w_s \bar{\delta} \varepsilon_0. \end{aligned} \quad (\text{A.8})$$

Eq. (A.8) can be solved for ε_0 to give the electrode surface gas fraction. For low values of $\varepsilon_0 \ll 1$, we get

$$\begin{aligned} \varepsilon_l &= \frac{\langle W_{g,c} \rangle}{\bar{\delta}(6w_p \bar{\delta}(k_1 - 2\bar{\delta}) + w_s)}, \\ \varepsilon_h &= \sqrt{\frac{\langle W_{g,c} \rangle}{6w_b \bar{\delta}^3(1 + k_2) - 3w_p(k_1 - \bar{\delta})}}. \end{aligned} \quad (\text{A.9})$$

A semi-analytical solution is obtained by solving Eq. (A.5) and Eq. (A.8) for ε_0 and w_p . However, an analytical approximation can also be obtained by using Eq. (B.5) and assuming $\bar{\delta}_c = \bar{\delta}_a = \bar{\delta}$ to give ε_0 and then solving Eq. (A.5) for w_p . The ε_0 obtained using Eq. (B.5) gives slightly lower values for ε_0 than the one obtained by simultaneously solving Eq. (A.5) and Eq. (A.8).

Natural Recirculation Velocity

For $Q < 2$, $\varepsilon_0 < 0.5$ and $\bar{\delta} < 0.5$, $k_1 \approx 1$, so that we can rewrite Eq. (A.4) for $\varepsilon_0 \bar{\delta} \ll 1$ and $\bar{\delta} \ll 1$ as

$$w_p = (1 + 6\varepsilon_0 \bar{\delta})\langle W \rangle - 6w_b \varepsilon_0 \bar{\delta}^2 (2 - \varepsilon_0 + k_2/2). \quad (\text{A.10})$$

We can again integrate w_p to get the total pressure drop as

$$\Delta P = -\frac{12\mu h \langle W \rangle}{l^2} \left(1 + \frac{6\varepsilon_0 \bar{\delta}_h}{1+a} \right) \left(1 - \left(\frac{\langle W \rangle_{nc}}{\langle W \rangle} \right)^{1+2b} \right), \quad (\text{A.11})$$

with

$$\langle W \rangle_{nc} \equiv \left(\frac{6w_b \varepsilon_0 (2 - \varepsilon_0 + k_2/2)}{(1 + 2a)(1 + 6\bar{\delta}\varepsilon_0/(1 + a))} \left(\frac{\mathcal{A}h^a}{l} \right)^2 \right)^{\frac{1}{1+2b}}. \quad (\text{A.12})$$

For $Q = 1$, $k_2 = 0$. We have an addition term, $\frac{6\bar{\delta}\varepsilon_0}{1+a}$ in Eq. (A.12) compared to Eq. (23) arising due to the non-constant relative viscosity μ_r . For $\Delta P = 0$, Eq. (A.11) gives the natural recirculation velocity as $\langle W \rangle = \langle W \rangle_{nc}$.

Expressions for different anode and cathode plume thickness

In our model, we have assumed equal plume thickness at the cathode and the anode. However, this assumption does not always hold, and the plume thickness can be different on the two sides, if the bubble diameter or volumetric gas flow rates are significantly different. In this section, we provide generalized expressions for different plume thicknesses $\bar{\delta}_a$ at the anode and $\bar{\delta}_c$ at the cathode, respectively so that Eq. (6) can be rewritten as:

$$\varepsilon = \varepsilon_0 \left(e^{-\frac{x}{\bar{\delta}_c}} + Q e^{-\frac{x}{\bar{\delta}_a}} \right). \quad (\text{B.1})$$

Assuming $\mu_m \approx \mu$ and solving Eq. 11 using Eq. (B.1) with no-slip boundary conditions for thin plumes compared to interelectrode gap ($e^{-1/\bar{\delta}_c} \ll 1$ and $e^{-1/\bar{\delta}_a} \ll 1$), we get

$$\begin{aligned} w &= 6w_p \bar{x}(1 - \bar{x}) \\ &\quad + 12w_b \varepsilon_0 \left(\bar{\delta}_c^2 \left(1 - \bar{x} - e^{-\frac{x}{\bar{\delta}_c}} \right) + Q \bar{\delta}_a^2 \left(\bar{x} - e^{-\frac{x}{\bar{\delta}_a}} \right) \right). \end{aligned} \quad (\text{B.2})$$

The average superficial velocity, $\langle W \rangle = \int_0^1 w(1 - \varepsilon)d\bar{x}$ using Eq. (B.2) for thin plumes with respect to interelectrode gap ($\bar{\delta}_a^2 \ll 1$, $e^{-1/\bar{\delta}_a} \ll 1$, $\bar{\delta}_c^2 \ll 1$ and $e^{-1/\bar{\delta}_c} \ll 1$), can be written as

$$\langle W \rangle = w_p + 6w_b \varepsilon_0 (\bar{\delta}_c^2 (1 - 2\bar{\delta}_c - \varepsilon_0 \bar{\delta}_c) + Q \bar{\delta}_a^2 (1 - 2\bar{\delta}_a - Q \varepsilon_0 \bar{\delta}_a)). \quad (\text{B.3})$$

where we assumed $w_p \ll w_b$. For $\bar{\delta}_a = \bar{\delta}_c = \bar{\delta}$, $\varepsilon_0 \bar{\delta} \ll 1$ and $Q = 1$, Eq. (B.3) reduces to Eq. (14). Using Eq. (B.2), we can rewrite Eq. (17) as

$$\langle W_{g,c} \rangle = 6w_b \bar{\delta}_c^2 (\bar{\delta}_c - 2\bar{\delta}_c^2 + 2Q \bar{\delta}_a^2) \varepsilon_0^2 + (6\bar{\delta}_c(1 - 2\bar{\delta}_c)w_p + w_s) \bar{\delta}_c \varepsilon_0. \quad (\text{B.4})$$

Solving Eq. (B.4) for ε_0 , we again obtain Eq. (21) with

$$\begin{aligned} \varepsilon_l &= \frac{\langle W_{g,c} \rangle}{\bar{\delta}_c(6w_p \bar{\delta}_c(1 - 2\bar{\delta}_c) + w_s)}, \\ \varepsilon_h &= \sqrt{\frac{\langle W_{g,c} \rangle}{6\bar{\delta}_c^2 (\bar{\delta}_c - 2\bar{\delta}_c^2 + 2Q \bar{\delta}_a^2) (1 - 12\bar{\delta}_c(1 - 2\bar{\delta}_c)^2) w_b}}. \end{aligned} \quad (\text{B.5})$$

Expressions for a step function gas fraction profile

In Fig. 9, we observed that at high current density, the plume is no longer exponential and attains more of a block-shape. In this appendix, we provide analytical expressions for velocity profiles and surface gas fraction, assuming a step function gas-fraction profile

$$\varepsilon = \begin{cases} \varepsilon_0, & x < \delta_b \\ 0, & \delta_b \leq x \leq l - \delta_b \\ \varepsilon_0, & l - \delta_b < x < l, \end{cases} \quad (\text{C.1})$$

where δ_b is the thickness of the plume. At the interface of the plume, we assume continuity of flow and shear stress. Using no slip conditions at the electrode surface and solving Eq. (11) for $\mu_r = \frac{1}{1-\varepsilon}$ using Eq. (C.1) gives

$$\begin{aligned} u &= 6w_p \bar{x}(1 - \bar{x}) \\ &\quad - 6\varepsilon_0 \begin{cases} w_p \bar{x}(1 - 2\bar{\delta}_b) + w_b \bar{x}(\bar{x} - 2\bar{\delta}_b), & x < \delta_b \\ w_p \bar{\delta}_b(1 - 2\bar{\delta}_b) - w_b \bar{\delta}_b^2, & \delta_b \leq x \leq l - \delta_b \\ w_p(1 - \bar{x})(1 - 2\bar{\delta}_b) + w_b(1 - \bar{x})(1 - \bar{x} - 2\bar{\delta}_b), & l - \delta_b < x. \end{cases} \end{aligned} \quad (\text{C.2})$$

Riviere and Cartellier (1999) took a similar approach for a more general gas fraction profile with an additional gas free layer near the electrode and a low gas fraction in the core with a higher gas fraction region between the two regions. In their analysis, they used a different closure model for shear stress giving $\varepsilon\mu_m$ instead of μ_m in Eq. (2).

The average superficial velocity using $\langle W \rangle = \int_0^1 u(1 - \varepsilon)d\bar{x}$ and Eq. (C.2) gives

$$\langle W \rangle = (1 - 6\varepsilon_0\bar{\delta}_b)w_p + 6w_b\varepsilon_0\bar{\delta}_b^2\left(1 - \frac{2\bar{\delta}_b}{3}\right). \quad (\text{C.3})$$

The average superficial gas velocity at the cathode $\langle W_{g,c} \rangle = \int_0^{\bar{\delta}_b} u\varepsilon_0 d\bar{x}$ can be written as

$$\langle W_{g,c} \rangle = \varepsilon_0^2\bar{\delta}_b^2(4\bar{\delta}_b w_b - 3w_p(1 - 2\bar{\delta}_b)) + \varepsilon_0\bar{\delta}_b(w_p\bar{\delta}_b(3 - 2\bar{\delta}_b) + w_s). \quad (\text{C.4})$$

Eq. (C.4) can be solved numerically to give the electrode surface gas fraction ε_0 . For low values of $\varepsilon_0 \ll 1$, we get

$$\varepsilon_0 = \frac{\langle W_{g,c} \rangle}{\bar{\delta}_b(w_p\bar{\delta}_b(3 - 2\bar{\delta}_b) + w_s)}, \quad (\text{C.5})$$

where w_p can be obtained for a given superficial liquid velocity using Eq. (C.3). Note that the expression for ε_0 is equal to that of Eq. (A.8) for $Q = 1$ upon replacing $6\delta(1 - 2\delta)$ with $3\bar{\delta}_b(1 - 2\bar{\delta}_b/3)$. It can be seen from Fig. 11 that for $j = 500 \text{ A/m}^2$, the exponential result of Eq. (A.8) gives satisfactory agreement with the numerical result, while for $j = 2000 \text{ A/m}^2$ Eq. (C.5) gives a slope similar to the numerical solution for the initial height of the electrode.

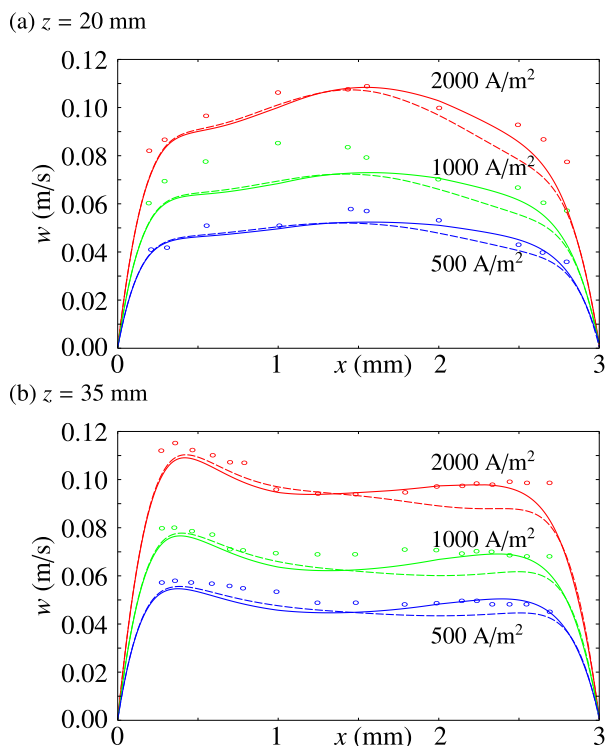


Fig. D.14. Gas phase velocity profiles for the three current densities: $j = 500 \text{ A/m}^2$ (blue), $j = 1000 \text{ A/m}^2$ (green), and $j = 2000 \text{ A/m}^2$ (red). The circles represent the experimental measurements from Boissonneau and Byrne (2000), the dashed line represents the numerical solution using the bubble diameter from Table 2 for both oxygen and hydrogen, and the solid line represents the numerical solution where the bubble diameters are different on the oxygen and the hydrogen side, and given by Eq. (D.1). We clearly see that accounting for different bubble sizes for hydrogen and oxygen gives a better agreement between the experiments and our numerical simulations.

Effect of Bubble Diameter

In Fig. 10, we see that velocities from numerical model shows deviation from the experimental results, particularly on the oxygen side because we assumed that oxygen bubbles are of similar size as the hydrogen bubbles. However, Boissonneau and Byrne (2000) suggest in their discussion that the plume on the oxygen side is larger than the plume on the hydrogen side. This may be due to the larger size of the oxygen bubble than the hydrogen bubble. Here, we shortly discuss the results with different bubble size for oxygen and hydrogen. The mixture Model in COMSOL allows only one dispersed phase and one continuous phase. In order to simulate different bubble size for oxygen and hydrogen, we use following distribution of bubble size in the horizontal direction

$$d_{b,\text{new}} = \begin{cases} d_b, & x \leq l/3 \\ d_b + \frac{0.5d_b}{l/3}(x - l/3), & l/3 < x < 2l/3 \\ 1.5d_b, & x \geq 2l/3 \end{cases}. \quad (\text{D.1})$$

Eq. (D.1) assumes that the oxygen bubbles are 50% bigger than the hydrogen bubbles. In the region $l/3 < x < 2l/3$ it is assumed that the diameter of dispersed phase bubbles increases from hydrogen bubble diameter to that of the oxygen bubble diameter linearly. As the bubble sizes are not reported for the oxygen side, we have used the same bubble size for both hydrogen and oxygen in the main text. Fig. D.14 shows a comparison between the dispersed phase velocity profiles using this approach to that reported by Boissonneau and Byrne (2000). We see that accounting for different bubble sizes for hydrogen and oxygen gives a better agreement between the experiments and our numerical simulations. This is because bigger bubbles provide larger buoyancy and terminal rise velocity.

References

- Aldas, K., Pehlivanoglu, N., Mat, M.D., 2008. *Int. J. Hydrogen Energy* 33, 3668–3675.
- Angulo, A., van der Linde, P., Gardeniers, H., Modestino, M., Rivas, D.F., 2020. *Joule* 4, 555–579.
- Atkinson, B., Brocklebank, M., Card, C., Smith, J., 1969. *AIChE J.* 15, 548–553.
- Baczynski, D., Weier, T., Kähler, C.J., Cierpka, C., 2015. *Exp. Fluids* 56, 1–13.
- Boissonneau, P., Byrne, P., 2000. *J. Appl. Electrochem.* 30, 767–775.
- Bongenaar-Schlechter, B.E., Janssen, L.J.J., Van Stralen, S.J.D., Barendrecht, E., 1985. *J. Appl. Electrochem.* 15, 537–548.
- Bruggeman, D., 1935. *Ann. Phys.* 416, 636–791.
- CFD Module User's guide v5.6, COMSOL, 2020.
- Clark, N.N., Flemmer, R.L., 1985. *Industr. Eng. Chem. Fundam.* 24, 412–418.
- L. Czarnetzki, Aspects of electrochemical production of hypochlorite and chlorate, Ph.D. thesis, Chemical Engineering and Chemistry, 1989. doi:10.6100/IR316966.
- Davis, J.T., Qi, J., Fan, X., Bui, J.C., Esposito, D.V., 2018. *Int. J. Hydrogen Energy* 43, 1224–1238.
- de Groot, M.T., Vreman, A.W., 2021. *Electrochim. Acta* 369, 137684.
- Eigeldinger, J., Vogt, H., 2000. *Electrochim. Acta* 45, 4449–4456.
- Esposito, D.V., 2017. *Joule* 1, 651–658.
- Esposito, D.V., Lee, Y., Yoon, H., Haney, P.M., Labrador, N.Y., Moffat, T.P., Talin, A.A., Szalai, V.A., 2017. *Sustain. Energy Fuels* 1, 154–173.
- Fukunaka, Y., Suzuki, K., Ueda, A., Kondo, Y., 1989. *J. Electrochem. Soc.* 136, 1002.
- Gillespie, M., Van Der Merwe, F., Kriek, R., 2015. *J. Power Sources* 293, 228–235.
- Goldberg, A., 2002. *Russ. J. Electrochem.* 38, 1025–1031.
- Groß, T., Bauer, J., Ludwig, G., Rivas, D.F., Pelz, P., 2018. *Exp. Fluids* 59, 1–10.
- Hadikhani, P., Hashemi, S.M.H., Schenk, S.A., Psaltis, D., 2021. *Sustain. Energy Fuels* 5, 2419–2432.
- Ham, J., Homsy, G., 1988. *Int. J. Multiphase Flow* 14, 533–546.
- Harada, S., Otomo, R., 2009. *Phys. Rev. E* 80, 066311.
- Hartmann, J., 1934. *Math. Phys. J.*, Copenhagen 15, 6.
- Hashemi, S.M.H., Modestino, M.A., Psaltis, D., 2015. *Energy Environ. Sci.* 8, 2003–2009.
- Haverkort, J.W., Rajaei, H., 2021. *J. Power Sources* 497, 229864.
- Hine, F., Murakami, K., 1980. *J. Electrochem. Soc.* 127, 292.
- Hine, F., Yasuda, M., Ogata, Y., Hara, K., 1984. *J. Electrochem. Soc.* 131.
- Holmes-Gentle, I., Hoffmann, F., Mesa, C.A., Hellgardt, K., 2017. *Sustainable Energy & Fuels* 1, 1184–1198.
- Hreiz, R., Abdelouahed, L., Fuenfschilling, D., Lopicque, F., 2015. *Chem. Eng. Sci.* 134, 138–152.
- Ishii, M., 1975. *NASA Sti/recon Technical Report A 75, 29657.*

- Ishii, M., Zuber, N., 1979. *AIChE J.* 25, 843–855.
- Jamshidi, R., Angeli, P., Mazzei, L., 2019. *Phys. Fluids* 31, 013302.
- Kellermann, H., Jüttner, K., Kreysa, G., et al., 1998. *Journal of applied electrochemistry* 28, 311–319.
- Kim, B.K., Kim, M.J., Kim, J.J., 1947. *ACS applied materials & interfaces* 13 (2021), 11940–11947.
- Koza, J.A., Mühlenhoff, S., Żabiński, P., Nikrityuk, P.A., Eckert, K., Uhlemann, M., Gebert, A., Weier, T., Schultz, L., Odenbach, S., 2011. *Electrochim. Acta* 56, 2665–2675.
- Kreysa, G., Kuhn, M., 1985. *Journal of applied electrochemistry* 15, 517–526.
- Krieger, I.M., Dougherty, T.J., 1959. *Transactions of the Society of Rheology* 3, 137–152.
- Krikke, I.R.C., 2021. Modeling the effect of dissolved gas on the bubble layer along a vertical gas evolving electrode Master's thesis. Delft University of Technology, The Netherlands.
- Kuroda, I., Sakakibara, A., Sasaki, T., Murai, Y., Nagai, N., Yamamoto, F., 2008. *Japanese Journal of Multiphase Flow* 22, 161–174.
- Landolt, D., Acosta, R., Müller, R.H., Tobias, C.W., 1970. *J. Electrochem. Soc.* 117, 839.
- Le Bideau, D., Mandin, P., Benbouzid, M., Kim, M., Sellier, M., Ganci, F., Inguanta, R., 2020. *Energies* 13, 3394.
- Lee, J.W., Sohn, D.K., Ko, H.S., 2019. *Exp. Fluids* 60, 1–11.
- Leighton, D., Acrivos, A., 1987a. *J. Fluid Mech.* 177, 109–131.
- Leighton, D., Acrivos, A., 1987b. *J. Fluid Mech.* 181, 415–439.
- Lessard, R.R., Zieminski, S.A., 1971. *Industrial & Engineering Chemistry Fundamentals* 10, 260–269.
- Li, Y., Fu, J., Geng, Z., Dong, H., 2022. *Int. J. Multiph. Flow* 147, 103918.
- M.D. Mat, K. Aldas, *International journal of hydrogen energy* 30 (2005) 411–420.
- McLaughlin, J.B., 1991. *Journal of fluid Mechanics* 224, 261–274.
- Mei, R., 1992. *Int. J. Multiph. Flow* 18, 145–147.
- Millet, P., Ngameni, R., Grigoriev, S., Fateev, V., 2011. *International journal of hydrogen energy* 36, 4156–4163.
- Müller, U., Bühler, L., 2001. *Magnetofluidynamics in Channels and Containers*. Springer, pp. 37–55.
- Nakoryakov, V., Kashinsky, O., Burdukov, A., Odnoral, V., 1981. *Int. J. Multiph. Flow* 7, 63–81.
- Nguyen, V., Papavassiliou, D.V., 2020. *Fluids* 5, 79.
- Nicolai, H., Herzhaft, B., Hinch, E., Oger, L., Guazzelli, E., 1995. *Phys. Fluids* 7, 12–23.
- Obata, K., Mokeddem, A., Abdi, F.F., 2021. *Cell Reports Physical Science*, 100358.
- O'Neil, G.D., Christian, C.D., Brown, D.E., Esposito, D.V., 2016. *Journal of The Electrochemical Society* 163, F3012.
- Orvalho, S., Stanovsky, P., Ruzicka, M.C., 2021. *Chem. Eng. J.* 406, 125926.
- Pang, X., Davis, J.T., Harvey, A.D., Esposito, D.V., 2020. *Energy & Environmental Science* 13, 3663–3678.
- Perkins, T., Johnston, O., 1963. *Soc. Petrol. Eng. J.* 3, 70–84.
- Rajaei, H., Rajora, A., Haverkort, J.W., 2021. *J. Power Sources* 491, 229364.
- Richardson, J., Zaki, W., 1954. *Chem. Eng. Sci.* 3, 65–73.
- Riegel, H., Mitrovic, J., Stephan, K., 1998. *Journal of applied electrochemistry* 28, 10–17.
- Riviere, N., Cartellier, A., 1999. *European Journal of Mechanics-B/Fluids* 18, 823–846.
- Rodríguez, J., Amores, E., 2020. *Processes* 8, 1634.
- Saffman, P., 1965. *Journal of fluid mechanics* 22, 385–400.
- Schillings, J., Doche, O., Deseure, J., 2015. *Int. J. Heat Mass Transf.* 85, 292–299.
- Schillings, J., Doche, O., Retamales, M.T., Bauer, F., Deseure, J., Tardu, S., 2017. *Int. J. Multiph. Flow* 89, 92–107.
- Sigrist, L., Dossenbach, O., Ibl, N., 1980. *Journal of applied electrochemistry* 10, 223–228.
- Suss, M.E., Conforti, K., Gilson, L., Buie, C.R., Bazant, M.Z., 2016. *RSC advances* 6, 100209–100213.
- Thorpe, J.F., Funk, J.E., Bong, T.Y., 1970. *J. Basic Eng.* 92, 173–182.
- Tong, W., Forster, M., Dionigi, F., Dresp, S., Erami, R.S., Strasser, P., Cowan, A.J., Farràs, P., 2020. *Nature Energy* 5, 367–377.
- Vafai, K., Kim, S.J., 1989. *ASME J. Heat Transfer* 111, 1103–1106.
- Vogt, H., 1982. *J. Appl. Electrochem.* 12, 261–266.
- Vogt, H., 1999. *Journal of applied electrochemistry* 29, 1155–1159.
- Vogt, H., 2011. *Electrochim. Acta* 56, 2404–2410.
- Wedin, R., Dahlkild, A.A., 2001. *Industrial & engineering chemistry research* 40, 5228–5233.
- Weier, T., Landgraf, S., 2013. *The European Physical Journal Special Topics* 220, 313–322.
- Zarghami, A., Deen, N., Vreman, A., 2020. *Chem. Eng. Sci.* 227, 115926.